https://doi.org/10.5194/esd-2019-78
Preprint. Discussion started: 6 January 2020

Earth System Dynamics
Discussions
Open Access
EGU

Precipitation Ansatz dependent Future Sea Level Contribution by Antarctica based on CMIP5 Model Forcing.

Christian B. Rodehacke[1,2], Madlene Pfeiffer[1], Tido Semmler[1], Özgür Gurses[1], and Thomas Kleiner[1]

[1]Alfred Wegener Institute Helmholtz Centre for Polar and Marine Research, D-27570 Bremerhaven, Germany
[2]Danish Meteorological Institute, DK-2100 Copenhagen Ø, Denmark

Correspondence: Christian Rodehacke (christian.rodehacke@awi.de)

Abstract. Various observational estimates indicate growing mass loss at Antarctica's margins but also heavier precipitation across the continent. In the future, heavier precipitation fallen on Antarctica will counteract any stronger iceberg discharge and increased basal melting of floating ice shelves driven by a warming ocean. Here, we use from nine CMIP5 models future projections, ranging from strong mitigation efforts to business-as-usual, to run an ensemble of ice-sheet simulations. We test, how the precipitation boundary condition determines Antarctica's sea-level contribution. The spatial and temporal varying climate forcings drive ice-sheet simulations. Hence, our ensemble inherits all spatial and temporal climate patterns, which is in contrast to a spatial mean forcing. Regardless of the applied boundary condition and forcing, some areas will lose ice in the future, such as the glaciers from the West Antarctic Ice Sheet draining into the Amundsen Sea. In general the simulated ice-sheet thickness grows in a broad marginal strip, where incoming storms deliver topographically controlled precipitation. This strip shows the largest ice thickness differences between the applied precipitation boundary conditions too. On average Antarctica's ice mass shrinks for all future scenarios if the precipitation is scaled by the spatial temperature anomalies coming from the CMIP5 models. In this approach, we use the relative precipitation increment per degree warming as invariant scaling constant. In contrast, Antarctica gains mass in our simulations if we apply the simulated precipitation anomalies of the CMIP5 models directly. Here, the scaling factors show a distinct spatial pattern across Antarctica. Furthermore, the diagnosed mean scaling across all considered climate forcings is larger than the values deduced from ice cores. In general, the scaling is higher across the East Antarctic Ice Sheet, lower across the West Antarctic Ice Sheet, and lowest around the Siple Coast. The latter is located on the east side of the Ross Ice Shelf.

Plain Language Summary In the warmer future, the ice sheet of Antarctica will lose more ice at the margin, because more icebergs may calve and the warming ocean melts more floating ice shelves from below. However, the hydrological cycle is also stronger in a warmer world. As a consequence, more snowfall precipitates on Antarctica, which may balance the amplified marginal ice loss. In this study, we have used future climate scenarios from various global climate models to perform numerous ice-sheet simulations. These simulations represent the Antarctic Ice Sheet. We analyze whether Antarctica will grow or shrink. In all our simulations, we find that certain areas will lose ice under all circumstances. However, depending on the method used to describe the precipitation reaching Antarctica in our simulations, parts of the Antarctic Ice Sheet may either grow or shrink in the future. How strong the precipitation grows in a warming atmosphere, may be explained by the dissimilarity between

https://doi.org/10.5194/esd-2019-78
Preprint. Discussion started: 6 January 2020


Earth System Dynamics Discussions
Open Access
EGU

the applied methods to describe the precipitation. Furthermore, the dissimilarity is pronounced differently between the West Antarctic and East Antarctic Ice Sheet.

1 Introduction

Sea level rise as a symptom of the progressing climate warming is of foremost importance for coastal societies because it impacts globally numerous economic activities and threatens the population along coasts. Antarctica's contribution to the future sea level is projected by either statistical approaches that take advantage of the deduced past behavior or dedicated model simulations of, for instance, ice-sheet models (Church et al., 2013). To run ice-sheet models, commonly simplified temporal forcing anomalies for the entire continent are applied on top of spatial background fields (e.g. Golledge et al., 2015; Winkelmann et al., 2012; Pollard and DeConto, 2009). Those background or reference fields are simplified descriptions by analytical equations (e.g., surface elevation and latitude dependence (Fortuin and Oerlemans, 1990)), come from regional climate models or climatological data sets. The simplified forcing, which usually does not show a dedicated spatial structure, follows some ad hoc assumed temporal evolution or is constructed from a set of CMIP5 model simulations, for instance. Here, we use various climate scenarios of an ensemble of CMIP5 models to drive the Parallel Ice Sheet Model (PISM, e.g. Bueler and Brown, 2009; Winkelmann et al., 2011), where we exploit the full temporal and spatial pattern in the atmospheric and oceanographic forcing. This approach is an enhancement to previous studies utilizing CMIP5 ensembles to infer only the temporal evolution of the future forcing (Golledge et al., 2015; Winkelmann et al., 2012).

The coupling between atmospheric warming and the enhanced hydrological cycle is often described as a Clausius-Clapeyron process, where the saturation pressure of water vapor scales exponentially by about $7\,\%$ per Kelvin warming (Held and Soden, 2006) — it is implicitly assumed that the relative humidity does not change. Climate modeling studies representing the Last Glacial Maximum (LGM), the pre-industrial (piControl) and historical period as well as climate warming scenarios (1pctCO2, abrupt4xCO2) show that the global precipitation increases in warmer climates and decreases in colder climates with a rate of $1\,\%\mathrm{K}^{-1}$ to $4\,\%\mathrm{K}^{-1}$ (Held and Soden, 2006; Li et al., 2013). Globally, this rate, which is the mean precipitation scaling, is less than the suggested thermodynamically justified Clausius-Clapeyron process for various reasons. Decreasing precipitation rates in the dry subtropics (Sun et al., 2007), covering a substantial part of the globe, limits the scaling. Dynamical and thermodynamical processes contribute both to the actual precipitation change, even if dynamical changes, such as an altering circulation, play a secondary role globally (Emori and Brown, 2005). The balance of radiative fluxes in/out of the troposphere and the latent energy flux at the surface limits evaporation, which restricts water vapor supply and ultimately the scaling (Allen and Ingram, 2002).

A global analysis of observed precipitation and temperature changes reveals a low or even negative scaling in tropical land regions driven by decreasing soil moisture, a near Clausius-Clapeyron scaling $\approx 7\%\mathrm{K}^{-1}$ over the open ocean, and a super Clausius-Clapeyron scaling ($>7\,\%\mathrm{K}^{-1}$) along extratropical coasts (Yin et al., 2018). In the latter case, the moisture supply by the ocean in concert with the atmospheric circulation generates extreme precipitation events inland. These events cause

https://doi.org/10.5194/esd-2019-78
Preprint. Discussion started: 6 January 2020


Earth System Dynamics Discussions Open Access EGU

high temperature scaling onshore. Ultimately, the local availability and recycling of moisture and the atmospheric dynamics determine the size of the precipitation-temperature scaling (Yin et al., 2018).

In Antarctica, global model simulations until the end of the century show an average scaling of about $7.4\,\%\mathrm{K}^{-1}$ (range: $5.5\,\%\mathrm{K}^{-1}$ – $24.5\,\%\mathrm{K}^{-1}$ Palerme et al., 2017), which is in agreement with CloudSat estimates (years 2007 – 2010, $7.1\,\%\mathrm{K}^{-1}$, Palerme et al., 2017). For the last deglaciation, global climate models suggest a value of about $6\,\%\mathrm{K}^{-1}$ in Antarctica, while future projections of a high-resolution regional climate model show a lower value of $4.9\,\%\mathrm{K}^{-1}$ in contrast to a higher value of $6.1 \pm 2.6\,\%\mathrm{K}^{-1}$ coming from an ensemble of global climate system models (Frieler et al., 2015). Ice core data covering 10,000 years of marked temperature changes reveal a value of $5 \pm 1\,\%\mathrm{K}^{-1}$ (Frieler et al., 2015). In standalone ice-sheet modeling studies, the commonly used temperature scaling factor for precipitation amounts to approximately $5\,\%\mathrm{K}^{-1}$ (e.g. Gregory and Huybrechts, 2006) in Antarctica, as the latitudinal relation obtained from a CMIP5 model ensemble suggests (Golledge et al., 2015). We consider $5\,\%\mathrm{K}^{-1}$ as the reference value further on.

While in most regions both the local availability and recycling of moisture and the atmospheric dynamics determine the size of the precipitation-temperature scaling (Yin et al., 2018), atmospheric dynamics dominate over the deep-frozen interior Antarctic continent probably due to negligible water buffering capacity of the frozen ground. The ocean surface conditions around Antarctica sets the lower boundary condition for the atmosphere, which accounts for the spread of the precipitation scaling among climate models. Atmosphere simulations over Antarctica, which are driven by boundary conditions from a small ensemble of historical and future climate scenarios, show a weak impact of changed atmospheric conditions or enhanced radiative forcing on the scaling factor (Krinner et al., 2014). In contrast, the ocean conditions are crucial for the precipitation scaling in Antarctica (Krinner et al., 2014). Sea ice cover has a decisive impact, where the mean historical sea ice concentration is more important than the sea ice retreat rate (Bracegirdle et al., 2015).

Across Antarctica, the patterns of increasing as well as decreasing precipitation are consistent with the variability of the large-scale moisture transport resembling the known Southern Hemispheric modes of variability, such as Amundsen Sea Low (ASL) or Southern Annular Mode (SAM) (Fyke et al., 2017). Also, the baroclinic annular mode (BAM) and the two Pacific-South American teleconnections (PSA1 and PSA2) indices influence precipitation over Antarctica (Marshall et al., 2017). An enhanced baroclinic annular mode, which corresponds to high storm amplitudes, increases the precipitation over the coastal East Antarctic Ice Sheet, while an enhanced SAM causes stronger precipitation across the West Antarctic Ice Sheet (WAIS) and the neighboring Antarctic Peninsula. The two Pacific-South American teleconnections impact mainly precipitation over the West Antarctic Ice Sheet beside other regions across the Antarctic continent.

In reanalysis products, no robust or statistically significant precipitation trend exists over Antarctica (Bromwich et al., 2011). This result is in agreement with precipitation observations over the Southern Ocean (Bromwich et al., 2011). However, shallow ice cores across Antarctica reveal a tendency for a positive precipitation trend over the last 50 years and 100 years. Since 1800, the increase of the surface mass balance (SMB) is $7 \pm 1.3\,\mathrm{Gt\,decade}^{-1}$ (Thomas et al., 2017).

In contrast, over the western region of the West Antarctic Ice Sheet (WAIS), next to the Ross Ice Shelf, a negative snow accumulation trend has been detected in monthly reanalysis products (ERA-Interim: 1979–2010 and ERA-20C: 1900–2010), which is confirmed by a composite of 17 firn cores (Wang et al., 2017). The flow of available atmospheric moisture, which

https://doi.org/10.5194/esd-2019-78
Preprint. Discussion started: 6 January 2020


Earth System Dynamics Discussions Open Access EGU

feeds the precipitation across the WAIS, is dominated by the Amundsen Sea Low (Thomas et al., 2017). A location shift of the Amundsen Sea Low (ASL), expressed by its longitudinal position, exposes different regions to the inland-directed circulation branch of moisture-rich air masses — on the eastern side of the Low's center — or isolates them from moisture supply due to the offshore directed circulation branch — on the western side. Furthermore, the deepening of the ASL enhances the cyclonic circulation, which strengthens precipitation — southeast of the Low's center — over the Antarctic Peninsula and eastern WAIS. However, less moisture-rich air masses reach the western WAIS, which ultimately leads to an accumulation deficit. Enlarged sea ice extent in the Ross Sea (Haumann et al., 2016; Liu, 2004) damps evaporation to the atmosphere. In contrast, a decreasing sea ice trend in the Amundsen Sea and Bellingshausen Sea (Haumann et al., 2016; Jacobs, 2006) enhances the moisture supply. To conclude, the observed accumulation reduction is driven by the deepening of the ASL and reinforced by a more extensive sea ice extent in the Ross Sea (Wang et al., 2017).

Processes governing the balance between mass gain and mass loss determine if Antarctica contributes to a rising sea level. Antarctica's surface mass balance controls mass gain, while mass loss occurs predominantly by ocean-driven basal melting of ice shelves and iceberg calving (Wingham et al., 2018). For individual ice shelves, the fraction between basal melting and iceberg calving ranges from $10\,\%$ to $90\,\%$ (Depoorter et al., 2013). Estimates about the total mass loss agree within the uncertainties, even if they range from $2200\,\mathrm{Gt\,year^{-1}}$ to $2800\,\mathrm{Gt\,year^{-1}}$ (Depoorter et al., 2013; Liu et al., 2015; Rignot et al., 2013). However, they differ in the relative contribution between basal melting and calving. The overall mass loss is either driven by a nearly equal share between calving ($1321 \pm 144\,\mathrm{Gt\,year^{-1}}$) and basal melting ($1454 \pm 174\,\mathrm{Gt\,year^{-1}}$) (Depoorter et al., 2013), or the basal melting ($1516 \pm 106\,\mathrm{Gt\,year^{-1}}$) contribution is twice as much as the calving ($755 \pm 24\,\mathrm{Gt\,year^{-1}}$) contribution (Liu et al., 2015). The surface mass balance is the difference between mass gain by precipitation — and here predominantly snowfall — and surface meltwater that runs off, because it is not refrozen nor retained in the snowpack. Surface melt ponds (Kingslake et al., 2017) and runoff exist on Antarctic ice shelves (Bell et al., 2017), but their contribution to the total mass balance is considered to be negligible (Van Wessem et al., 2014), except for the (northern) Antarctic Peninsula (Adusumilli et al., 2018).

The focus of this paper is to identify common features of an ensemble of ice-sheet simulations forced by a multimodel forcing ensemble. After the discussion on the temporal and spatial evolution of the climatic boundary conditions from nine CMIP5 models, we diagnose the temperature scaling of the precipitation of these climate models. Afterwards, we investigate how the deduced scaling impacts the global sea level in contrast to spatially homogeneous scaling, e.g inferred from ice core data. The impact of these precipitation conditions on simulated ice-sheet thickness is analyzed before we attribute the climate models, which cause extreme changes. Before we conclude, we estimate differences in Antarctica's sea-level contribution for the variety of applied forcing and precipitation boundary conditions.

2 Material and Methods

The full temporally and spatially varying forcings are obtained from an ensemble of CMIP5 models representing a suite of climate scenarios. These climate forcings drive the Parallel Ice Sheet Model (PISM) in order to estimate Antarctica's future

https://doi.org/10.5194/esd-2019-78
Preprint. Discussion started: 6 January 2020


Earth System Dynamics Discussions

sea-level contribution. In particular, the Ansatz of the precipitation determines whether the global sea level rises or falls. We consider two precipitation boundary conditions. (1) On top of the reference background distributions (see Table 2), which drive the ice-sheet model during the spin-up, we utilize both the temperature and the precipitation anomalies from CMIP5 models. (2) We take only the temperature anomalies from CMIP5 models and compute the precipitation anomalies scaled by the temperature anomalies. The latter is common (Applegate et al., 2012; Bakker et al., 2016; de Boer et al., 2013, e.g), while some keep the surface mass balance constant (Feldmann and Levermann, 2015; Hughes et al., 2017). In some cases, negative temperature scaling is considered unrealistic (Frieler et al., 2012).

Nine CMIP5 models deliver the following climate scenarios (see Table 1): control run (piControl), the historical period (1850-2005), as well as RCP2.6, RCP4.5, and RCP8.5 (2006-2100). These models stem from different model families (Knutti et al., 2013) and cover the range of current atmospheric (Agosta et al., 2015) and oceanographic (Sallée et al., 2013a) model uncertainties although model deficiencies such as insufficient resolution can exist across all models. The transient forcing from 1850 until 2100 comprises the historical and scenario periods. Afterward, the last 30 years (2071-2100) are repeated until the year 5000 to keep the natural variability. From the control run of the climate model (piControl), we use either the first or the last 50 years. By this procedure, we could quickly identify a drift in CMIP5 models and assess its impact. Additionally, the number of scenarios is twice as large, since the mean states of the first and last 50 years differ commonly marginally. Anomaly forcing is computed relative to either the first or last 50 years of the control run. In the following, the first 50 years act generally as reference.

Atmospheric and oceanic forcing is applied as annual mean forcing on top of the forcing used to spin-up the ice-sheet model (Table 2). Since CMIP5 models do not resolve ice shelves, ocean temperatures are extrapolated horizontally into the ice shelves to mimic isopycnical flow. To allow for surface melting under a warming climate, the surface mass balance (SMB) is calculated following the positive degree day (PDD) approach (Braithwaite, 1995; Hock, 2005; Ohmura, 2001), where the annual 2m-air temperature standard deviation comes from daily CMIP5 model values.

The ice-sheet model PISM — based on version 0.7 — runs on a 16 km equidistant polar stereographic grid and it utilizes a hybrid system combining the Shallow Ice Approximation (SIA) and Shallow Shelf Approximation (SSA). The model utilizes a generalized version of the viscoelastic Lingle-Clark bedrock deformation model (Bueler et al., 2007; Lingle and Clark, 1985). In our simulations, only the viscous part has been used because of known implementation flaws in the elastic part in our and later PISM versions. The basal resistance is described as plastic till by a Mohr-Coulomb formula to perform the yield stress computation (Bueler and Brown, 2009; Schoof, 2006). The basal melting of ice shelves is proportional to the squared thermal temperature forcing ($\Delta T^2_{\mathrm{force}}$), which is the difference between the pressure-dependent melting temperature and the actual ocean temperature above melting. Here, the parameterization considers the full depth-dependence of the ocean temperature field, as described in Sutter et al. (2019). Basal ice-shelf melting occurs only in fully floating grid points, while the grounding line position is determined on a sub-grid space (Feldmann et al., 2014).

The calving occurs at the ice-shelf margin, and three sub-schemes determine it. (1) At the ocean-ice-shelf margin, ice-shelf grid points with a thickness of less than $150\,\mathrm{m}$ calve. (2) Ice shelves calve that extend across the continental shelf edge and progress into the depth ocean (defined by the $1500\,\mathrm{m}$ depth contour). (3) The Eigen-calving parameterization exploits the

https://doi.org/10.5194/esd-2019-78
Preprint. Discussion started: 6 January 2020


Earth System Dynamics Discussions

stress field divergence (Levermann et al., 2012), with the proportionality constant of either $1 \cdot 10^{17}$ or $1 \cdot 10^{18}$. Two independent spin-up runs delivering our initial conditions (PISM1Eq and PISM2Eq) utilize these constants. Ocean temperatures from the World Ocean Atlas 2009 (Locarnini et al., 2010) and the multi-year mean surface mass balance (SMB) from the RACMO 2.3/ANT model (Van Wessem et al., 2014) drive PISM during spin-up (Table 2). A similar model setup has taken part in the initMIP-Antarctica exercise under the name AWI_PISM1Eq with an adjusted Eigen-calving proportionality constant of $2 \cdot 10^{18}$ and no bed deformation (Seroussi et al., 2019a).

3 Results and Discussions

Depending on the applied CMIP5 forcing scenario, the ensemble mean climate signal is weaker for those scenarios following an aggressive mitigation path and, hence, releasing less carbon dioxide. Around Antarctica, the here analyzed ensemble follows the same pattern (Figure 2 and Figure 3). Since in the past decade greenhouse gas concentrations have followed most closely the RCP8.5 scenario path, we will focus on RCP8.5 if not otherwise stated.

3.1 Ensemble Forcing

From 1850 until the end of the 21st century, the ensemble mean 2m-air temperature in Antarctica (see the map of Figure 3d) rises steadily by $6\,\mathrm{K}$ with a spread of $1\,\mathrm{K}$ (one standard deviation) (Figure 3a) while the mean precipitation accumulates $9 \pm 3\,\mathrm{cmyear}^{-1}$ (water equivalent) in addition (Figure 3b). The average potential ocean temperature in the depth range of $150\mathrm{m}$ to $500\mathrm{m}$ depth along Antarctica's coast (see the map of Figure 3e) warms by nearly $1 \pm 0.18°\mathrm{C}$ (Figure 3c). In particular, since the beginning of 21st century, these increases become stronger.

These changes are not homogeneous across the Antarctic continent (Figure 2d-l). The atmosphere warms strongest along the Antarctic Peninsula (Mulvaney et al., 2012; Thomas et al., 2009, in agreement with current trends), the high plateau of the East Antarctic Ice Sheet (EAIS) and to a lesser degree around the Filchner-Ronne-Ice Shelf region (Figure 2d, g, j). The warming is lowest in the coastal areas of East and West Antarctica that extend (clockwise) from the Greenwich Meridian via Wilkens Land and the Ross Ice Shelf to the Marie Byrd Land, respectively, where the Amery Ice Shelf interrupts this coastal band of moderate temperature rises. Please note that the inland coastal areas of the West Antarctic Ice Sheet (WAIS), the Wilkens Land, and the region between the Greenwich Meridian and the Antarctic Peninsula (western Weddell Sea) warms less than the adjacent ocean and ice-sheet interior.

The precipitation increases marginally across the high plateau of the EAIS and east of the Ross Ice Shelf as part of the WAIS (Figure 2e, h, k). In contrast, the coastal areas, where air masses with much precipitable water make landfall, receive more precipitation. Since these air masses on their way into the interior are uplifted by the steep topography, the precipitation along the coasts is topographically controlled. Areas of heavy precipitation under the reference climate (Figure 2b) also receive the highest increments. The precipitation increases strongest along the western Antarctic Peninsula, where the lifting of eastward flowing air masses by mountain ranges leads to topographic precipitation, which is firmly enhanced; this resembles the observed positive precipitation trend of the Antarctic Peninsula since 1900 (Wang et al., 2017).

https://doi.org/10.5194/esd-2019-78
Preprint. Discussion started: 6 January 2020


Earth System Dynamics Discussions
Open Access
EGU

Under the control climate, the coldest potential ocean temperatures in the depth range from $150\,\mathrm{m}$ to $500\,\mathrm{m}$ exist offshore the coasts of Antarctica (Figure 2c). We detect the lowest temperatures in front of the Filchner-Ronne, Amery, and Ross Ice Shelves. Also, the Amundsen Sea in front of Pine Island Glacier and Thwaites Glacier is cold. Here, the temperature might be too cold, which justifies the applied melting correction.

The subsurface ocean-temperature warms vigorously along sections of the Antarctic Circumpolar Current (ACC) and in the western Weddell Sea at the center of the ocean gyre. For instance, the warm spot in the western Weddell Sea emerges in all ensemble members (Figure 2f, i, l). In the coastal strip surrounding Antarctica, the warming is of medium strength and heterogeneous. There, most robust warming appears in the Amundsen Sea and along the coast of the EAIS (between Wilkens Land and Terre Adélie) opposite of Australia. Least warming occurs in front of both the western Ross Ice and Filchner-Ronne Ice Shelves and the neighboring Antarctic Peninsula, where the ocean temperatures are lowest in the control climate (Figure 2c).

The spatial structure of the anomalies discussed above is in general independent of the applied forcing scenario, while the scenarios determine, however, the strength of the anomalies. Regardless of the applied scenario, the discussion of the atmospheric climate anomalies indicates already that both precipitation and temperature do not necessarily grow in parallel. Instead, regional differences are evident, and a simple scaling of the precipitation with temperature appears to be inadequate.

3.2 Precipitation scaling

Inspired by the Clausius-Clapeyron process, it is often assumed that with a warming atmosphere, the precipitation also raises. ice-sheet simulations bridging several millennia often rely on climate anomalies deduced from ice cores, for instance. Based on isotopic signatures in ice cores, temperature anomalies are deduced. Inferred accumulation anomalies from these cores are converted into precipitation anomalies. Together with the contemporary climate fields as a reference, the temperature scaling of precipitation is

$$S(t,\boldsymbol{x}) = \Delta T(t,\boldsymbol{x}) \frac{\Delta P(t,\boldsymbol{x})}{P_{t=0}(\boldsymbol{x})} \cdot [100\%], \tag{1}$$

where ΔT is the temperature anomaly, ΔP the precipitation anomaly, and $P0 = P(t_{\mathrm{ref}})$ the precipitation reference field. The scaled precipitation is

$$P(t,\boldsymbol{x}) = \Delta P(t,\boldsymbol{x}) \; [1 + \Delta T(t,\boldsymbol{x}) \cdot S(t,\boldsymbol{x})] \,.$$

The scaling deduced from ice cores varies in Antarctica between $5\,\%\mathrm{K}^{-1}$ and $7\,\%\mathrm{K}^{-1}$, with a 2-sigma uncertainty of about $1\,\%\mathrm{K}^{-1} - 3\,\%\mathrm{K}^{-1}$ (Figure 4, Table 3).

The corresponding scaling of the ensemble mean is generally larger at these locations. The difference is distinct for Vostok and, to a less degree, also for EDML and EDC, while, within the uncertainties, the scaling of the Law Dome, Talos Dome, and WAIS ice cores are indistinguishable from the corresponding ensemble means. Here, we have computed the scaling by averaging the precipitation of the piControl run (first 50 years) to obtain the reference data and the last 50 years of the RCP8.5 scenario from 2051 until 2100 to get the anomalies. If we replace the reference period by the first 50 years of the historical

https://doi.org/10.5194/esd-2019-78
Preprint. Discussion started: 6 January 2020


Earth System Dynamics Discussions Open Access EGU

period (1850-1899), the results are similar, and the values change only slightly. Thus, we can safely restrict the analysis on the first 50 years.

The spatial distribution of the scaling derived from our ensemble data is spatially heterogeneous and varies stronger than the ice core data suggest. Values in the range between $4\,\%\mathrm{K}^{-1}$ and $6\,\%\mathrm{K}^{-1}$ occur at the Filchner-Ronne Ice Shelf and in the coastal Terre Adélie region (see Map 1 for place names). Furthermore, as part of the WAIS these values are present in the coastal strip from the Antarctic Peninsula to the Ross Ice Shelf and along the eastern flank of the Transantarctic Mountain Range (Figure 4).

The highest scaling factor emerges on the EAIS, where a c-like area as part of the high plateau has factors exceeding $12\,\%\mathrm{K}^{-1}$. This area reaches out to the Dronning Maud Land with very high scaling factors too. The West Antarctic Ice Sheet has scaling factors generally lower than $8\,\%\mathrm{K}^{-1}$ and only on the elevated interior values up to $10\,\%\mathrm{K}^{-1}$ are detected. Over the Ross Ice Shelf and the eastward adjacent Siple Coast, scaling factors are the lowest (Figure 4). Since we detect raised scaling factors at a higher elevation, we aimed at determining whether we could find a relationship between elevation and scaling. However, neither for the entire Antarctic continent nor for defined subregions (see below), we could identify any robust relationship (not shown).

Our analysis focuses now on the scaling factors of all grounded ice, which, if lost, contributes to a rising sea level by Antarctica. Additionally, we analyze the scaling factors for the entire continent (label “glaciered”), and four glaciated regions labeled “EAIS Atl”, “EAIS Ind”, “WAIS”, and “Siple Coast” (Figure 5 and Table 4). We detect a slight trend to higher values if we restrict the analysis to ground ice. However, the difference between scenarios is more decisive than the choice between “glaciered” and “grounded” for the ensemble mean as well as for numerous individual ensemble members (e.g., CCSM4, CanESM2, HadGEM2-ES, NorESM1-M). Within their variability, many ensemble members are invariant against the applied scenario (e.g., CSIRO-Mk3-6-0, CNRM-CM5, MIROC-ESM, MRI-CGCM3) or may hint at an enlarged scaling for weaker scenarios (e.g., MPI-ESM-LR). Frieler et al. (2015) found a low dependence of the scaling factors to four RCP scenarios for the whole Antarctic continent. Anomalies are not as distinctly pronounced in RCP2.6 as in the other scenarios due to the weaker forcing scenario. Please note, that CCSM4 is missing in the RCP2.6 (hence we have hatched the corresponding bar).

The boundaries of the three regions “EAIS Atl”, “EAIS Ind”, and “WAIS” resemble different oceanographic zones under the consideration of Antarctica’s large-scale drainage basins. This division of Antarctica does not produce surface area of equal size. As already indicated by the spatial distribution (Figure 4), the ordering from high to low scaling factors would be “EAIS Atl”, “EAIS Ind”, and “WAIS”. The difference between both “EAIS” regions is minor, with a tendency of higher values in “EAIS Atl” in the ensemble mean and some individual ensemble members. Some ensemble members do not show a clear trend between the scenario strength and scaling factor. For example, for MRI-CGCM3 the scaling decreases in “EAIS Atl” from RCP4.5 over RCP8.5 to RCP2.6, while in “EAIS Ind” the order is different from RCP8.5, RCP2.6, to RCP4.5 (Figure 5). It indicates again, that regional differences matter.

The region “WAIS” has significantly lower scaling factors than both “EAIS” regions. This difference exists for all ensemble means regardless of the applied scenarios and for almost all individual ensemble members (Figure A3), except some individual ensemble members under the RCP2.6 scenario (MIROC-ESM, MPI-ESM-LR) and the HadGEM2-ES.

https://doi.org/10.5194/esd-2019-78
Preprint. Discussion started: 6 January 2020


Earth System Dynamics Discussions

The region "Siple Coast" as a part of the "WAIS" region is different in many aspects. It has the smallest area compared to the other regions (Table 4), and it shows the lowest ensemble mean scaling factors for all scenarios. Also, as before, no clear trend exists between different scenarios across the entire ensemble, while the spread of trends among individual ensemble members is substantial. Furthermore, some members exhibit a negative scaling, where precipitation decreases for rising temperatures: MPI-ESM-LR under the RCP8.5 scenario and NorESM1-M under all scenarios (RCP8.5, RCP4.5, and RCP2.6). The inverted sign of the scaling is in stark contrast to the ensemble mean.

In the last decades, the detected downward trend in snow accumulation in this area (Wang et al., 2017) occurs while the wider West Antarctic Ice Sheet region belongs to the most rapidly warming regions globally (Bromwich et al., 2012). It underpins that less accumulation can befall under a warming climate. Furthermore, sea ice has expanded in the Ross Sea (Haumann et al., 2016; Liu, 2004). Hence, some ensemble members seem to imitate that expanding sea ice modifies the evaporation from the ocean and impacts the atmospheric circulation, which controls the flow of humid air masses, delivering precipitation to the Siple Coast. Even if NorESM1-M reproduces the overall seasonal sea ice extent cycle better than most CMIP5 models (Turner et al., 2013), it shows a unrealistic declining February sea ice trend in the Ross Sea over 1979-2005 (Turner et al., 2013). MPI-ESM-LR has large negative errors in sea ice extent over the year (Turner et al., 2013). Hence the mimicry of observed features in models may occur for the wrong reason.

In all four large regions ("glaciered", "grounded", "EAIS Atl", "EAIS Ind", and "WAIS"), we see a trend towards lower scalings for weaker forcing scenarios in the ensemble mean, with the exception of "EAIS Ind", where the factors for RCP8.5 and RPC4.5 are indistinguishable. Also, Frieler et al. (2015) found a low dependence of the scaling factors to the RCP scenario in comparison with the dependence on the specific climate model. The region "WAIS" has on average a smaller precipitation scaling than both regions of the East Antarctic Ice Sheet ("EAIS Atl" and "EAIS Ind"), which is also reflected by the maxima in these regions. Also, the Ross Ice Shelf and the adjacent Siple Coast feature on average the lowest scaling factors across the entire ice sheet. Some individual ensemble members project even negative scaling: precipitation deficit for rising temperatures.

The Siple Coast highlights definitely that, at the continental scale, it is not adequate to describe the spatial evolution of the precipitation by a fixed temperature scaling. Since the scaling exceeds mostly the commonly utilized value of $5\,\%\mathrm{K}^{-1}$, for instance, we diagnose the sea-level impact of applying the actual scaling distribution (e.g., Figure 4) versus a spatially and temporally constant scaling of $2\,\%\mathrm{K}^{-1}$, $5\,\%\mathrm{K}^{-1}$, or $8\,\%\mathrm{K}^{-1}$ across Antarctica.

3.3 Sea Level Impact of Precipitation Scaling by Temperature

To understand how the precipitation boundary condition impacts Antarctica's contribution to the global sea level, we inspect the precipitation fallen on Antarctica (Figure 6). Therefore, we integrate it over the dark-blue masked region of grounded ice (map on Figure 6), perform a cumulative summation since 1850, and restrict our analysis to all ensemble members driven by RCP8.5 (and anomalies relative to the first 50 years of the control run). Since accumulated precipitation over Antarctica lowers the global sea level under the assumption that ice loss (basal melting or calving) does not occur, the temporally accumulated sea-level impact curves have a negative slope (Figure 6a, b). Further on, this quantity is labeled "integrated precipitation," and the presented sea-level equivalent assumes a global ocean area of $3.61 \cdot 10^{14}\mathrm{m}^2$ (Gill, 1982).

https://doi.org/10.5194/esd-2019-78
Preprint. Discussion started: 6 January 2020


Earth System Dynamics Discussions Open Access EGU

The integrated precipitation declines more forcefully since the beginning of the 21st century, which is driven by the concurrent increase of precipitation over Antarctica (Figure 3a). The integrated precipitation shows a more pronounced temporal change, because the integral and not the mean precipitation is calculated, where the vast light precipitation regions lessen the average precipitation signal. After the year 2100, the integrated precipitation declines linearly (Figure 6b), as we adopt the forcing of the years 2071-2100 recurrently. By applying the actual precipitation anomalies (solid lines, Figure 6a, b), the sea-level drop is stronger than using a scaling of $5\,\%\mathrm{K}^{-1}$ (dashed lines, Figure 6b) because the models' internal scaling exceeds $5\,\%\mathrm{K}^{-1}$ (Figure 5). Thus, in the year 5000, the maximal sea-level drop of $11\,\mathrm{m}$ (CCSM4) is nearly twice as large under the precipitation anomalies, compared to less than $6\,\mathrm{m}$ (MIROC-ESM) for the $5\,\%$ scaling.

The difference of the integrated precipitation between $5\,\%\mathrm{K}^{-1}$ scaled and directly applied precipitation anomalies is always positive (solid lines in Figure 6 c, d). This difference ranges approximately from $1\,\mathrm{cm}$ (CISRO-Mk3-6-0) to $15\,\mathrm{cm}$ (CCSM4) in the year 2100 and from $60\,\mathrm{cm}$ (MPI-ESM-LR) to $550\,\mathrm{cm}$ (CCSM4) in the year 5000. A lower scaling of $2\,\%\mathrm{K}^{-1}$ causes a magnified difference (dotted line in Figure 6 c, d), which corresponds to a reduced sea-level impact if we would apply this low scaling of $2\,\%\mathrm{K}^{-1}$. It leads to differences ranging from $5\,\mathrm{cm}$ (MPI-ESM-LR) to $21\,\mathrm{cm}$ (CNRM-CM5) in 2100 and from $150\,\mathrm{cm}$ (MPI-ESM-LR) to $850\,\mathrm{cm}$ (CCSM4) in 5000.

A higher scaling of $8\,\%\mathrm{K}^{-1}$ (dashed line in Figure 6c, d) exceeds ice core-based estimates (Table 3, Figure 4), while it corresponds approximately to the ensemble mean (RCP8.5 $\approx 8.2\,\%\mathrm{K}^{-1}$, RCP4.5 $\approx 7.8\,\%\mathrm{K}^{-1}$, Figure 5). Now, only the CCSM4 model exhibits a positive difference because its scaling reaches $11\,\%\mathrm{K}^{-1}$ (Figure 5). Four models are nearly balanced (CNRM-CM5, MRI-CGCM3, HadGEM2-ES, NorESM1-M), while the remaining four feature negative differences (CISRO-Mk3-6-0, CanESM2, MIROC-ESM, MPI-ESM-LR). Hence, the difference range is subject to a change of sign, and the individual differences range from $-5\,\mathrm{cm}$ (CISRO-Mk3-6-0) to $7\,\mathrm{cm}$ (CCSM4) in 2100 and from -170 cm (CISRO-Mk3-6-0) to 280 cm (CCSM4) in 5000.

Over the entire Antarctic continent, precipitation and temperature grow simultaneously in climate model simulations of the future. In concert with estimates of accumulation changes and temperature anomalies obtained from ice cores, it may (mis)lead us to scale the precipitation by the temporally evolving temperature. Therefore, fixed scaling factors are common. However, a tendency towards higher scaling exists under more vigorous climate trends (Figure 5), and the scaling has a clear spatial dependence (Figure 4 and 5). As a consequence, the on Antarctica accumulated snowfall for future climate projections differs between the methods, which ultimately leads to biased estimates of Antarctica's contribution to the global sea level. To assess the introduced bias, we analyze simulations of the Parallel Ice Sheet Model driven with numerous variants of the above-discussed climate conditions and a diverse set of implemented boundary conditions.

3.4 Relation between Precipitation Boundary Condition and Ice Thickness

Starting in the year 1850, we performed numerous ice-sheet simulations to analyze how the implemented precipitation boundary condition impacts the ice-sheet thickness distribution. Each climate scenario from an individual climate model (as part of the ensemble) drives an independent ice-sheet simulation. These together constitute the ensemble of ice-sheet simulations. Hence, the average across ice-sheet simulations forms the ensemble mean. For the diagnostic, we also inspect the maximum and

https://doi.org/10.5194/esd-2019-78
Preprint. Discussion started: 6 January 2020

minimum thickness at each grid point across all ensemble members. Therefore, the field of joined extreme values could come from a diverse set of ice-sheet ensemble members and, hence, does not necessarily lead to dynamically consistent distribution.

Complementary ice-sheet (control) simulations are performed under the sole utilization of the reference forcing fields (Figure 2a-c). In these simulations, the detected trend of about $2\,\mathrm{mm\,decade^{-1}}$ (sea-level equivalent) fades within the first 400 years and differs slightly between the two initial states (PISM1Eq and PISM2Eq). Hence, in the following, the subtracted trend for each single ensemble member depends on its initial state.

In the year 2100, the ice thickness for both precipitation boundary conditions (precipitation anomaly deduced from the applied climate models versus scaled precipitation) increase over large parts of the Antarctic continent (Figure 7b-e). The thickness for the simulations driven by scaled precipitation grows less over substantial parts of the interior than the simulations forced by the precipitation anomalies (Figure 7a) as the difference between scaled precipitation and applied precipitation anomaly is mostly negative. Thus, simulations driven by the precipitation anomalies accumulate more snow and grow thicker ice, which leads to a stronger sea-level drop. This result supports the analysis above (Figure 6). A ring of a pronounced negative thickness difference follows the coast, where the precipitation anomaly (Figure 2e, h, k) is enhanced. This ring emerges for a significant part of the coastal East Antarctic Ice Sheet (EAIS) and West Antarctic Ice Sheet (WAIS). For the latter ice sheet, the negative area is shifted away from the coast towards the interior (Figure 7a). Also, a negative strip appears at the south side of the Transantarctic Mountain Range, and some grounded ice streams flowing into the Filchner-Ronne Ice Shelf are negative.

Regions of positive differences coincide with thicker ice for simulations driven by scaled precipitation. These are located south of the Transantarctic Mountain Range at the northern edge of the Ross Ice Shelf, along the coastline of the WAIS, and in the coastal Terre Adélie region. There, the scaling is generally lower or falls behind the constant scaling of 5% K-1. However, this does not explain exclusively positive areas.

For both precipitation boundary conditions, the ice thicknesses of the ensemble means reveal a widespread weakening of the floating ice shelves, such as Filchner-Ronne, Ross, and Amery Ice Shelves (Figure 7b, d). In the WAIS, both Pine Island Glacier and Ferrigno Ice Stream (an ice stream that flows into the Filchner Ice Shelf) thin drastically. Along the Antarctic Peninsula, general shrinking occurs along the coasts. Also along the marginal EAIS, ice thins.

For some places, the ice thickness thins for both precipitation boundary conditions across all ensemble members as the reduction of the maximal ice thickness highlights (Figure 8c, e). This reduction marks those outlet glaciers and ice shelves that are extremely vulnerable. These are around the Rutford Ice Stream, Foundation Ice Stream, Ronne Ice Shelf, Amery Ice Shelf, three outlet glaciers (in "EAIS Ind" as part of Wilkens Land, Terre Adélie, and George V Land), northwestern Ross Ice Shelf (Ross Island), and Pine Island together with Thwaites Glacier in the Amundsen Sea (Figure 8c, e).

To conclude, the ice thickness is indeed thicker for simulations driven by the precipitation anomalies (Figure 8). Regardless of the applied precipitation boundary condition, there is widespread ice-shelf weakening, ice thinning at the margins in the ensemble mean. Ice thinning for the ensemble member of the maximal thickness highlights the most vulnerable regions, such as Pine Island and Thwaites Glaciers, Amery Ice Shelf and some outlet glaciers of the EAIS.

https://doi.org/10.5194/esd-2019-78
Preprint. Discussion started: 6 January 2020


Earth System Dynamics Discussions
Open Access
EGU

3.5 Attribution of the driving model

All ensemble members contribute to the ensemble mean, while at a given grid location the maximum and minimum are determined by climate forcing from one particular climate model. We inspect which climate model may lead to ice thickness growth or shrinking and restrict ourselves first to the model year 2100, where the precipitation anomalies of the period 1850–2100 shape the ice-sheet thickness distribution of the year 2100.

Directly at margins apart from the vast ice shelves, the attributed model that drives either the maximum or minimum ice thickness shows a noisy small scale pattern, which is driven by the variety of the involved models (Figure 8d, e). The mean and minimum thicknesses of the Filchner-Ronne and Ross Ice Shelves, and also to some extent the Amery Ice Shelf, are highlighted by a nearly unique color patch indicating a reduced thickness. These patches are separated from the surroundings showing either a reduced thinning or even thickening. Intriguingly, the MIROC-ESM model, for instance, causes thicker grounded ice east and west of the Ross Ice Shelf (Figure 8d), while it also drives its thinning of the Ross Ice Shelf (Figure 8e) predominantly. Hence, the ocean forcing drives the ice-shelf thinning here. Since the spatial pattern of the atmospheric and ocean forcing that promotes or undermines the ice thickness is not necessarily aligned, this may explain the small scale noisy pattern along the coast.

Beyond the direct coast strip, larger areas appear where the forcing from one climate model determines the maximum or minimum thickness, respectively. However, these extended continuous regions are often interrupted by spots controlled by the climate from other models. Also, the pattern is changing during the transient simulation starting in 1850 because the temporal evolution of the 2m-air temperature and precipitation anomalies are different for each climate model as the integrated precipitation highlights (Figure 6a, b). Furthermore, after the year 2100, where the same 30 years forcing period (2071–2100) drives the ice-sheet model recurrently, the pattern evolves further (Figure 9). Because the ice sheet has not reached the quasi-equilibrium to the last 30 years forcing, the pattern alteration is ongoing.

For grounded ice, three models (CCSM4, CNRM-CM5, MIROC-ESM) determine predominantly the growing ice until the year 2100 (Figure 8d), which is in-line with the diagnosed sea-level contribution (solid line, Figure 6a, b). CCSM4 dominates the “EAIS Atl” sector, while CNRM-CM5 dominates a band from the “EAIS Ind” sector clockwise to the Antarctica Peninsula, which is interrupted by regional-scale patches of the MIROC-ESM. A spatial dominance is not apparent for the minimum ice thickness, because the patchwork of five models (CSIRO-Mk3-6-0, HadGEM2-ES, MPI-ESM-LR, MRI-CGCM3, NorESM1-M) dominates the year 2100. NorESM1-M influences the WAIS, which is in accordance with the detected lowest scaling in the Siple Coast (Figure 5), CSIRO-Mk3-6-0 has an impact around the South Pole, MRI-CGCM3 has coastal zone in the EAIS, while the control of MPI-ESM-LR and, to a lesser extent, HadGEM2-ES spreads across the entire continent. If we progress into the year 2200, where we have applied the 30 years forcing more than three times, the emerging picture shows a consolidation of the influential spheres of the different models for both the maximum and minimum thicknesses (Figure 9).

If we now turn towards the temperature scaled model simulations, the mean, maximum, and minimum ice thickness distributions (Figure 10) are similar to the ones driven by the precipitation anomalies as discussed above (Figure 7). Also, the same models determine the ice-shelf thickness of the Filchner-Ronne and Ross Ice Shelves. The latter shows that the ocean

https://doi.org/10.5194/esd-2019-78
Preprint. Discussion started: 6 January 2020


Earth System Dynamics Discussions

controls ice-shelf thickness changes in our simulations primarily. However, we detect a stark contrast of the model determining the maximum and minimum ice thickness. For the maximum, we still have the same three models (CCSM4, CNRM-CM5, MIROC-ESM). However, the pattern has changed. CCSM4 controls a smaller area in the interior around the South Pole, and MIROC-ESM some coastal regions of the East Antarctic Continent, while the remaining majority of the grounded ice is under the control of CNRM-CM5. The most striking changes occur for the minimum. Now, NorESM1-M determines the entire WAIS and some parts of "EAIS Ind", while MRI-CGCM3 dominates the remaining East Antarctic Ice Sheet.

In the latter case, temperature variations force the precipitation driven ice thickness evolution exclusively (see Equation 1). These temperature changes do not necessarily reflect dynamical changes in the atmosphere that are accompanied by modified circulation patterns that ultimately transport and deliver the precipitation for Antarctica. Hence, the applied scaling or precipitation boundary condition impacts the temporal evolution of the Antarctic Ice Sheet geometry, which ultimately shapes Antarctica's contribution to the global sea level.

3.6 Ice losses

After the spin-up, the simulations have reached a quasi-equilibrium. For the discussion of the ice losses, we concentrate on the transient period 1850-2100. The calving rate hardly changes (Figure A12), whereas the total ice-shelf area is nearly constant until 2000 and declines afterward (Figure A15). The ocean-driven basal melting is proportional to the squared temperature difference between the pressure-dependent melting temperature and the actual ocean temperature. Since the ocean temperature increases in general (Figure 2f, i, l and Figure 3c), also the mass loss by basal melting increases, while the total shelf ice area is quasi-constant until 2000 and declines afterward (Figure A15). For RCP8.5, the basal melting increases at the end of the 21st century quadratic. To conclude, the calving rate is nearly constant, while the basal melting increases by approximately $33\,\%$ since the year 2000.

The mean calving rate is about $8000\,\mathrm{Gt\,year^{-1}}$ and $5000\,\mathrm{Gt\,year^{-1}}$ for the ensemble member utilizing the parameters and the initial state of PISM1Eq and PISM2Eq, respectively (Figure A12). The basal melting rates for PISM1Eq and PISM2Eq are similar, however, the loss rates for PISM1Eq are slightly larger than PISM2Eq (Figure A13). The ensemble mean starts at about $550\,\mathrm{Gt\,year^{-1}}$ in 1850 and reaches $900\,\mathrm{Gt\,year^{-1}}$ in 2100.

Since floating ice shelves nourish both ice losses, these ice losses do not impact the sea-level directly. Under the assumption that the inflow of former grounded ice compensates any shelf mass loss, the reported ice losses of $8500\,\mathrm{Gt\,year^{-1}}$–$9000\,\mathrm{Gt\,year^{-1}}$ (5500–$6000\,\mathrm{Gt\,year^{-1}}$) would correspond to a sea-level rise of $2.58\,\mathrm{cm\,year^{1}}$–$2.74\,\mathrm{cm\,year^{1}}$ ($1.67\,\mathrm{cm\,year^{1}}$–$1.83\,\mathrm{cm\,year^{1}}$). The Integration over 250 years to match the period from 1850 to 2100 generates a sea-level equivalent of $6.47\,\mathrm{m}$ – $6.85\,\mathrm{m}$ ($4.19\,\mathrm{m}$ – $4.57\,\mathrm{m}$). However, the actual ratio between total ice mass change and the corresponding sea level response is not a 1:1 relation. Instead, on average less than $5\,\%$ of the total mass lost by both iceberg calving and floating ice-shelf melting is compensated by grounded ice that raises the sea level (Figure A8). Considering this ratio of $5\,\%$, the sea level impact reduces to $0.32\,\mathrm{m}$ – $0.34\,\mathrm{m}$ ($0,21\,\mathrm{m}$ – $0.23\,\mathrm{m}$). It is less than integrated precipitation anomalies across the Antarctic continent (Figure 6a).

https://doi.org/10.5194/esd-2019-78
Preprint. Discussion started: 6 January 2020


Earth System Dynamics Discussions Open Access EGU

Anyhow, the integrated basal melting rates are too low and the calving rates are too high compared to observational estimates in our ensemble of ice-sheet model simulations. Besides the fact that the total loss exceeds recent observational estimates, our ice sheet is in a quasi-equilibrium after the spin-up. All this may indicate that the integrated precipitation driven accumulation resulting from the RACMO precipitation reference field might be too large. However, the surface mass balance of RACMO agrees well with observational estimates (Wang et al., 2016), while the uncertainty of the surface mass balance (sea-level equivalent of $\sim 0.25\,\mathrm{mm\,year^{-1}}$ (Van Wessem et al., 2014)) is of almost the same size as Antarctica's sea-level contribution ($\sim 0.2\,\mathrm{mm\,year^{-1}}$ between 1992 and 2011 (Shepherd et al., 2012; Wang et al., 2016)). Additionally, recent satellite-based estimates indicate clearly that the Antarctica Ice Sheet loses mass (sea-level equivalent: $0.4\,\mathrm{mm\,year^{-1}}$) in the period 2011–2017 (Sasgen et al., 2019).

Beyond the year 2100 (Figure A14), the calving rates decrease and reach a minimum in the period 3000–4000. Afterward, calving increases again slightly. Basal melting rates are subject to a slight decreasing trend (RCP2.6), nearly constant values (RCP4.5), or a negligible upward trend after the year 4000 (RCP8.5).

3.7 Precipitation Boundary condition and Sea Level

In the following, we consider all ensemble members starting from both initial states PISM1Eq and PISM2Eq. They are driven by the climate scenarios RCP2.6, RPC4.5, or RCP8.5. For each CMIP5 model, the applied anomalies have been computed either relative to the first or last 50 years of the control run simulation (piControl). The sea-level curves are shifted so that the sea-level contribution is $0\,\mathrm{m}$ in the year 2000. Since the spread of individual ensemble members may not follow a normal distribution, we present beside the mean also the median sea-level contribution. For the RCP8.5 scenario, we highlight the spreading among models by depicting the standard deviation (1σ).

For the period 1850 until 2000, the simulated sea level contribution of Antarctica fluctuates slightly. Hence, the accumulation balances nearly the ice loss at the margin while the basal melting rated of grounded ice is steady (Figure A9). Please note that this is not driven by any trend in the continued ice-sheet simulations under the reference climate (Table 2) since we have subtracted this trend. We also detect an amplified signal for the simulations driven by the precipitation anomalies than scaled precipitation, which corresponds to the above diagnosed sea-level impact of the precipitation (Figure 6).

After the year 2000, all our ensemble members, regardless of the forcing scenario, show a falling sea level (Figure 12). The basal melting of grounded ice does not impact the sea level contribution, because this basal melting rate, expressed as integrated sea-level equivalent since 1850, is the same and grows linearly for all scenarios until 2100, and only after the year 2500 these curves diverge (Figure A9). Ultimately, the more vibrant growth of the accumulation in comparison to the negligible increasing combined loss of iceberg calving and basal melting of ice shelves drive the falling sea level in our simulations after the year 2000 (Figure 12). Depending on the applied forcing and precipitation boundary condition, the global sea-level drop ranges from $2\,\mathrm{cm}$ to $11\,\mathrm{cm}$ until 2100 (Figure 12). This result is in contrast to various publications, and we discuss it below.

If we continue our ensemble with the last 30 years of forcing until the year 5000, the sea-level contribution of those ensemble members driven by the temperature scaled precipitation starts to stabilize and reaches a minimum around the year 2500. Afterward, they begin to lose more ice at the margins than they gain in the interior. As a consequence, these will contribute

https://doi.org/10.5194/esd-2019-78
Preprint. Discussion started: 6 January 2020


Earth System Dynamics Discussions Open Access EGU

after the year 3200 (RCP8.5) and 3900 (RCP2.6) to a globally rising sea level on average in our simulations, which outruns the formerly fallen sea level since 1850. In the year 5000 at the end of our simulations, these runs show a trend towards a continuously growing ice loss rate, because the curves have still an upward-directed tendency. Hence a quasi-equilibrium is not established. In contrast, the simulations driven by the precipitation anomalies continue to show a falling sea level. They always contribute negatively to the global sea until the year 5000, and their ensemble mean and median sea levels tend to converge at the end of the simulations.

3.7.1 Sea level contribution of corrected basal melting

Since the deduced Antarctica's sea level contribution disagrees with the currently observed state showing mass loss, we apply a corrected time series representing the observational-based ocean-driven basal melting. These time series preserve the fluxes' amplification over time, which is essentially the ratio of the higher end value to the lower start value. Hence, the corrected basal melt flux replicates the original simulated amplification while the flux is identical to the observed reference value ($F_{\mathrm{ref}}(t_{\mathrm{ref}})$) at the reference time (t_{ref}). Under the assumption that only a fraction of the adjusted basal mass contributes to the global sea level, we apply the simulated ratio of the sea level change to the total ice mass change. For each ensemble member, this ratio is the median ratio over its entire time series (For details inspect please the appendix section "Bias-corrected fluxes" A3 on page 46). Since we examine enhanced mass loss, we do not adjust the iceberg calving rates that are already higher than observed.

The determined temporal evolution of the sea level correction (Figure A5, Equation A8) does impact the global sea level, but it does not change the sign of the contemporary sea-level evolution. Consequently, the impact on the sea level is very small as its evolution, which considers the correction, highlights (Figure A6). If we assume instead that all of the additional mass loss of floating ice shelves rises the sea level immediately, we obtain too extensive corrections of $30\,\mathrm{cm}$ between 1850 and 2000. This sea-level rise is larger than the observed integrated sea level rise of about $20\,\mathrm{cm}$ since 1850 (Church and White, 2011), which has been driven by world-wide land-water storage changes, shrinking glaciers around the globe, enhanced melting from Greenland, and thermal expansion of the ocean (Cazenave and Remy, 2011; Leclercq et al., 2011; Church and White, 2011).

To conclude: The correction exceeds observational estimates significantly under the unrealistic assumption that all additional basal melting of ice shelves raises the sea level. It is unrealistic because disintegrating floating ice shelves do not impact the sea level. The correction hardly corrects the discrepancy if we apply the inferred ration of about $5\,\%$ between the simulated total ice mass loss and the simulated sea level contribution.

4 Conclusions

It is crucial for numerical simulations of Antarctica's sea-level contribution, how the precipitation is implemented in ice-sheet simulations. The commonly used method of scaling the precipitation changes with the simulated temperature changes from ice cores or global climate models leads to a positive Antarctic sea-level contribution, i.e., a sea-level rise. However, when considering the simulated precipitation changes from the global climate models, the situation changes. In this case, numerical projections simulate a negative sea-level contribution. Major uncertainties affect these simulations, such as the partitioning of

https://doi.org/10.5194/esd-2019-78
Preprint. Discussion started: 6 January 2020

ice losses into calving and basal melt — which is quite different from observational estimates due to very crude representations in the ice-sheet model — or the omission of important processes, such as the ocean-ice-shelf-ice-sheet interactions. While we could improve some aspects of the involved process descriptions, our simulations are state-of-the-art and suffer, thence, the same limitations as others.

In all CMIP5 models, the 2m-air temperature warms across the entire Antarctic continent without any exception (Figure 2d, g, j, and 3a), because even the minimum 2m-air temperature anomaly is positive everywhere (Appendix Figure A2d, g, j). The warming enhances the hydrological cycle, which causes generally heavier precipitation (Figure 3b) in particular along the coast of Antarctica (Figure 2e, h, k). However, the changing precipitation does not increase at the same rate with increasing temperature because it is not only thermodynamically influenced but also dynamically controlled. Given that the ensemble mean temperature scaling is different for the West and East Antarctic Ice Sheet (Figure 5) and has a considerable spatial dependence, the dynamical component is not negligible. Instead, the region of reduced precipitation under rising air temperatures, which we have identified along the Siple Coast, highlights that the dynamics could compensate or even overwhelm the thermodynamics. The continent-wide scaling is per se problematic, even if we would adjust the scaling factor to reproduce the continental-wide average scaling. In this case, the total amount would be identical, but the spatial structure is still entirely different (Figure 4). Hence for a proper projection of Antarctica's sea-level contribution, the spatial pattern of the future accumulation of precipitation shall also consider the dynamical effect.

Independent of the applied precipitation boundary condition, we detect regions where the ice thickness thins for all ensemble members. These regions are the Amundsen Sea Embayment with both Pine Island and Thwaites Glaciers, some outlet glaciers of the East Antarctic Ice Sheet (EAIS) between George V and Wilkens Land, Amery Ice Sheet, and the Northern Antarctica Peninsula. These regions correspond to those, which have been identified across sixteen models, where ocean warming wanes marginal ice (Seroussi et al., 2019a).

The ocean (Etourneau et al., 2019) and atmosphere (Mulvaney et al., 2012; Thomas et al., 2009; Morris and Vaughan, 2003) is already warming along the Antarctic Peninsula. This results in a southward progressing of the annual 2m-air temperatures of -9°C or -5°C isotherm, which presents the range of thresholds for the stability of ice shelves suggested by Morris and Vaughan (2003, -9°C) and Doake (2001, -5°C), respectively. It may also enable the formation of meltwater ponds on ice shelves (Kingslake et al., 2017) that precedes (van den Broeke, 2005) or even triggers ice-shelf disintegration (Banwell et al., 2013, 2019). After an ice shelf has decayed, the feeding ice streams are losing more ice, as seen for Larsen-B (Rott et al., 2011), which lowers the thickness of grounded ice. Anyhow, ice shelves along the Antarctic Peninsula have collapsed or are retreating (Cook and Vaughan, 2010; Rott et al., 1996). This observed retreat and the related ice loss will continue in our simulations under RCP8.5.

For part of the EAIS, simulations show that grounded ice of the Wilkens Basin in the hinterland of George V Land may be prone to a massive ice loss if the ice front loses its buttressing effect (Mengel and Levermann, 2014). Our ensemble shows, on average, a stable situation here. Ice in deep troughs that are in contact with the warming ocean thins at some spots further to the west. It happens in front of the Astrolabe Trench (in Terre Adélie) and on the coast of the Wilkens Land, for example near the Totten Glacier. Ice also thins in the deep trench leading to the Amery Ice Shelf.

https://doi.org/10.5194/esd-2019-78
Preprint. Discussion started: 6 January 2020

Both the Pine Island and Thwaites Glaciers in the Amundsen Sea as part of the marginal West Antarctic Ice Sheet (Jeong et al., 2016; Milillo et al., 2019; Rignot et al., 2014; Scambos et al., 2017) lose ice. For them, continuous ice loss is inevitable according to our simulations. Also, the Ferringo Ice Stream flowing into the Bellingshausen Sea will thin in the future.

Since our simulations presented here are in contrast to others that project a sea-level contribution from a shrinking Antarctic Ice Sheet, we highlight the differences before we discuss the limitations of our simulations. Some simulate Antarctica with a finer spatial resolution (Golledge et al., 2015; Pollard et al., 2015), which could improve the presentation of ice streams. These streams channelize the flow of grounded ice from the interior to the margins, where they feed the attached ice shelves and discharge directly into the ocean. However, the simulated surface velocity distribution reproduces appropriate satellite-based estimates (Appendix Figure A10 and Figure A11). Others used the cliff failure parameterization supporting ice loss together with a constant ocean temperature offset of +2°C (Pollard et al., 2015), twice as large as the amount found in our ensemble of nine CMIP5 models (Figure 3), or utilized continuously raising atmospheric and oceanographic temperature forcing (Golledge et al., 2015; Mengel et al., 2015; Winkelmann et al., 2012, 2015) beyond the year 2100. These stronger forcings alone explain a large part of the difference because we apply recurrently the forcing of the years 2071–2100 after 2100.

Since the precipitation boundary condition determines if Antarctica rises or lowers the global sea level, it may be appropriate to utilize a more sophisticated surface mass balance (SMB) model. The recent publication that indicates a Greenlandification of Antarctica's margin at the end of the century (Bell et al., 2018) supports this approach, but the required atmospheric inputs fields are not available at sufficient temporal resolution. Hence, this will be an option for simulations driven by the forthcoming CMIP6 model output.

Even if we apply anomalies on top of the reference background fields, we can not exclude a shock-like behavior of the simulations entirely directly following the decades after the year 1850. Since we compute the anomalies relative to the first or last 50 years, respectively, of the control run for each climate model, the anomalies are not necessarily zero at the beginning of the year 1850. Hence, the ice-sheet model may experience a small jump, which may cause a wrong trend initially. Nevertheless, the long-term positive and negative sea-level contribution of Antarctica for simulations driven by temperature scaled and directly applied precipitation anomalies, respectively, are robust.

An issue could be the parameterization of the grounding line migration, where only extremely high resolution relaxes its need. However, PISM's grounding line parameterizations at medium to lower resolution is consistent with higher-order models (Feldmann et al., 2014). It explains that the present-day grounding line position resembles the current state reasonably, and the simulated grounding line retreat follows the bulk of simulations in the last model intercomparison (Seroussi et al., 2019a); hence, we consider our grounding line migration as reasonable. The apparent stability of ice shelves in the runs driven by the precipitation anomalies seems to comply with the safety band of ice shelves (Fürst et al., 2016), so the calving does stay outside of ice-shelf regions essential for providing buttressing for the inflowing grounded ice streams.

The ocean boundary condition, where ocean conditions are extrapolated into the ice-shelf cavities, drive basal ablation of ice shelves. Here, we could undoubtedly improve simulations if the ice shelves would be coupled to the driving ocean model, so that basal melting impacts the thermal structure of the ocean and, ultimately, the melt patterns. CMIP5 models neglect the ocean-ice-shelf interaction (Meijers, 2014), and their coarse resolution around Antarctica does not allow to represent the regional

https://doi.org/10.5194/esd-2019-78
Preprint. Discussion started: 6 January 2020

conditions (Heuzé et al., 2013; Sallée et al., 2013b). They are subject to unrealistic open-ocean convection (Heuzé et al., 2013; Meijers, 2014; Sallée et al., 2013a) instead of convection on or near the continental shelf (Årthun et al., 2013; Nicholls et al., 2009). All these taint the hydrographic structure along Antarctica's coasts. Hence, any improved parameterization can not rectify the existing biases in the ocean forcing. These biases are reduced if we apply ocean temperature anomalies on top of an observational-based climatological data set as performed in our study.

Since we extrapolate coastal ocean temperatures laterally into the ice-shelf cavities, the obtained ocean warming might be higher if we would include the rise of the strongly warming gyre centers. If this may have been incorporated in the forcing of other groups obtaining a higher ice loss, depends on the setup details. However, it may help to bridge the gap between other studies and our simulations.

Nevertheless, the detected sea-level decrease for the used precipitation anomaly forcing is in agreement with a growing surface mass balance since 1800 AD, driven mainly by the Antarctic Peninsula region (Thomas et al., 2017). During intensive El Nino years, the accumulation-driven ice height increase between Dotson Ice Shelf and Ross Ice Shelf exceeds the height reduction by basal melting processes (Paolo et al., 2018), but the ice mass is still decreasing since the low-density snowfall replaces ice with a higher density. The stability arguments of Ritz et al. (2015) confirm the apparent stability of Antarctica in our simulations. Furthermore, various recent ice-sheet model simulations, driven by selected CMIP5 climate model fields in the framework of the ISMIP6 exercise, are subject to a negative sea-level contribution under a warming climate (Seroussi et al., 2019b).

To evaluate the impact of the precipitation boundary condition, fully coupled simulations between a dynamic ice-sheet/shelf model and a global climate model are inevitable. The system would include the ice-shelf-ocean interaction of coupled ocean-ice shelves at a sufficiently high spatial resolution around Antarctica. In addition, it would contain a sophisticated surface mass balance computation. We hope these coupled atmosphere-ocean/sea-ice–ice-sheet/shelf models will overcome the discussed limitations.

Code and data availability. The Code of the Parallel Ice Sheet Model is freely available from https://github.com/pism/pism. Modifications of the PISM's code are available from TK upon reasonable request. The data is available from the corresponding author or TS upon reasonable request.

Author contributions. CR performed the simulations and wrote the manuscript. All authors contributed to the interpretation of the results and proofreading of the manuscript.

Competing interests. The authors declare that they have no conflict of interest.

https://doi.org/10.5194/esd-2019-78
Preprint. Discussion started: 6 January 2020

Acknowledgements. This work has been financed through the German Federal Ministry of Education and Research (Bundesministerium für Bildung und Forschung: BMBF) project ZUWEISS (grant agreement 01LS1612A). Parts of this work are supported by BMBF grant 01LP1503B (project PalMod1.2). The Deutsche Klima Rechenzentrum (DKRZ) supplied computer resources on the cluster "mistral". CR wants to thank the AWI's HPC administrators for their proactive and generous support enabling this work during the development phase. The development of PISM is supported by NASA grant NNX17AG65G and NSF grants PLR-1603799 and PLR-1644277. The data analyzes and the production of figures have been predominantly performed with the help of the following software products (alphabetic order): Climate Data Operators (CDO: https://code.mpimet.mpg.de/projects/cdo/), Generic Mapping Tools (GMT: https://www.generic-mapping-tools.org/), Ncview (http://meteora.ucsd.edu/~pierce/ncview_home_page.html), netCDF Operator (NCO, http://nco.sourceforge.net/), PyFerret (https://ferret.pmel.noaa.gov/Ferret/documentation/pyferret), python (python3, https://www.python.org/, including the following packages NumpPy: https://numpy.org, matplotlib: https://matplotlib.org, and xarray: https://xarray.pydata.org/). We thank the numerous authors and their financial supporters of these software products.

https://doi.org/10.5194/esd-2019-78
Preprint. Discussion started: 6 January 2020

Earth System Dynamics Discussions

References

Adusumilli, S., Fricker, H. A., Siegfried, M. R., Padman, L., Paolo, F. S., and Ligtenberg, S. R. M.: Variable Basal Melt Rates of Antarctic Peninsula Ice Shelves, 1994-2016, Geophysical Research Letters, 45, 4086–4095, https://doi.org/10.1002/2017GL076652, 2018.

Agosta, C., Fettweis, X., and Datta, R.: Evaluation of the CMIP5 models in the aim of regional modelling of the Antarctic surface mass balance, The Cryosphere, 9, 2311–2321, https://doi.org/10.5194/tc-9-2311-2015, 2015.

Allen, M. R. and Ingram, W. J.: Constraints on future changes in climate and the hydrologic cycle, Nature, 419, https://doi.org/10.1038/nature01092, 2002.

Applegate, P., Kirchner, N., Stone, E., Keller, K., and Greve, R.: An assessment of key model parametric uncertainties in projections of Greenland Ice Sheet behavior, The Cryosphere, 6, 589–606, https://doi.org/10.5194/tc-6-589-2012, 2012.

Årthun, M., Holland, P. R., Nicholls, K. W., and Feltham, D. L.: Eddy-Driven Exchange between the Open Ocean and a Sub–Ice Shelf Cavity, Journal of Physical Oceanography, 43, 2372–2387, https://doi.org/10.1175/JPO-D-13-0137.1, 2013.

Bakker, P., Clark, P. U., Golledge, N. R., Schmittner, A., and Weber, M. E.: Centennial-scale Holocene climate variations amplified by Antarctic Ice Sheet discharge, Nature, pp. 1476–4687, https://doi.org/10.1038/nature20582, 2016.

Banwell, A. F., MacAyeal, D. R., and Sergienko, O. V.: Break-up of the Larsen B Ice Shelf Triggered by Chain-Reaction Drainage of Supraglacial Lakes, Geophysical Research Letters, 40, 5pp, https://doi.org/10.1002/2013GL057694, 2013.

Banwell, A. F., Willis, I. C., Macdonald, G. J., Goodsell, B., and MacAyeal, D. R.: Direct measurements of ice-shelf flexure caused by surface meltwater ponding and drainage, Nature Communications, 10, 730, 10p, https://doi.org/10.1038/s41467-019-08522-5, 2019.

Bell, R. E., Chu, W., Kingslake, J., Das, I., Tedesco, M., Tinto, K. J., Zappa, C. J., Frezzotti, M., Boghosian, A., and Lee, W. S.: Antarctic ice shelf potentially stabilized by export of meltwater in surface river, Nature, 544, 344–348, https://doi.org/10.1038/nature22048, 2017.

Bell, R. E., Banwell, A. F., Trusel, L. D., and Kingslake, J.: Antarctic surface hydrology and impacts on ice-sheet mass balance, Nature Climate Change, 8, 1044–1052, https://doi.org/10.1038/s41558-018-0326-3, 2018.

Bracegirdle, T. J., Stephenson, D. B., Turner, J., and Phillips, T.: The importance of sea ice area biases in 21st century multimodel projections of Antarctic temperature and precipitation, Geophysical Research Letters, 42, 10,832–10,839, https://doi.org/10.1002/2015GL067055, 2015.

Braithwaite, R. J.: Positive degree-day factors for ablation on the Greenland Ice-sheet studied by energy balance modeling, Journal of Glaciology, 41, 153–160, http://apps.isiknowledge.com.proxy.lib.umich.edu/full{_}record.do?product=WOS{&}search{_}mode=GeneralSearch{&}qid=48{&}SID=1FH@LoL1EM39J5IMpgJ{&}page=1{&}doc=1, 1995.

Bromwich, D. H., Nicolas, J. P., and Monaghan, A. J.: An Assessment of Precipitation Changes over Antarctica and the Southern Ocean since 1989 in Contemporary Global Reanalyses, Journal of Climate, 24, 4189–4209, https://doi.org/10.1175/2011JCLI4074.1, 2011.

Bromwich, D. H., Nicolas, J. P., Monaghan, A. J., Lazzara, M. A., Keller, L. M., Weidner, G. A., and Wilson, A. B.: Central West Antarctica among the most rapidly warming regions on Earth, Nature Geoscience, 6, 139–145, https://doi.org/10.1038/ngeo1671, 2012.

Bueler, E. and Brown, J.: Shallow shelf approximation as a "sliding law" in a thermomechanically coupled ice sheet model, Journal of Geophysical Research, 114, 21pp, https://doi.org/10.1029/2008JF001179, 2009.

Bueler, E., Lingle, C. S., and Brown, J.: Fast computation of a viscoelastic deformable Earth model for ice-sheet simulations, Annals of Glaciology, 46, 97–105, https://doi.org/10.3189/172756407782871567, 2007.

Cazenave, A. and Remy, F.: Sea level and climate: measurements and causes of changes, Wiley Interdisciplinary Reviews: Climate Change, 2, 647–662, https://doi.org/10.1002/wcc.139, 2011.

https://doi.org/10.5194/esd-2019-78
Preprint. Discussion started: 6 January 2020

Church, J., Clark, P., Cazenave, A., Gregory, J., Jevrejeva, S., Levermann, A., Merrifield, M., Milne, G., Nerem, R., Nunn, P., Payne, A., Pfeffer, W., Stammer, D., and Unnikrishnan, A.: Sea Level Change, in: Climate Change 2013: The Physical Science Basis. Contribution of Working Group I to the Fifth Assessment Report of the Intergovernmental Panel on Climate Change, edited by Stocker, T., Qin, D., Plattner, G.-K., Tignor, M., Allen, S., Boschung, J., Nauels, A., Xia, Y., Bex, V., and Midgley, P., chap. 13, Cambridge University Press, Cambridge, UK and New York, NY, USA, http://www.ipcc.ch/report/ar5/wg1/, 2013.

Church, J. A. and White, N. J.: Sea-Level Rise from the Late 19th to the Early 21st Century, Surveys in Geophysics, 32, 585–602, https://doi.org/10.1007/s10712-011-9119-1, 2011.

Cook, A. J. and Vaughan, D. G.: Overview of areal changes of the ice shelves on the Antarctic Peninsula over the past 50 years, The Cryosphere, 4, 77–98, https://doi.org/10.5194/tc-4-77-2010, 2010.

de Boer, B., van de Wal, R. S. W., Lourens, L. J., Bintanja, R., and Reerink, T. J.: A continuous simulation of global ice volume over the past 1 million years with 3-D ice-sheet models, Climate Dynamics, 41, 1365–1384, https://doi.org/10.1007/s00382-012-1562-2, 2013.

Depoorter, M., Bamber, J., Griggs, J., Lenaerts, J., Ligtenberg, S., van den Broeke, M., and Moholdt, G.: Calving fluxes and basal melt rates of Antarctic ice shelves., Nature, 502, 89–92, https://doi.org/10.1038/nature12567, 2013.

Doake, C.: Ice-shelf Stability, in: Encyclopedia of Ocean Sciences, edited by Steele, J. H., Thorpe, S. A., and Turekian, K. K., January 1995, pp. 1282–1290, Elsevier, Amsterdam, https://doi.org/10.1006/rwos.2001.0005, 2001.

Emori, S. and Brown, S. J.: Dynamic and thermodynamic changes in mean and extreme precipitation under changed climate, Geophysical Research Letters, 32, 1–5, https://doi.org/10.1029/2005GL023272, 2005.

Etourneau, J., Sgubin, G., Crosta, X., Swingedouw, D., Willmott, V., Barbara, L., Houssais, M.-n., Schouten, S., Damsté, J. S. S., Goosse, H., Escutia, C., Crespin, J., Massé, G., and Kim, J.-H.: Ocean temperature impact on ice shelf extent in the eastern Antarctic Peninsula, Nature Communications, 10, 304, https://doi.org/10.1038/s41467-018-08195-6, 2019.

Feldmann, J. and Levermann, A.: Collapse of the West Antarctic Ice Sheet after local destabilization of the Amundsen Basin, Proceedings of the National Academy of Sciences, 112, 14 191–14 196, https://doi.org/10.1073/pnas.1512482112, 2015.

Feldmann, J., Albrecht, T., Khroulev, C., Pattyn, F., and Levermann, A.: Resolution-dependent performance of grounding line motion in a shallow model compared with a full-Stokes model according to the MISMIP3d intercomparison, Journal of Glaciology, 60, 353–360, https://doi.org/10.3189/2014JoG13J093, 2014.

Fortuin, J. and Oerlemans, J.: Parameterization of the Annual Surface Temperature and Mass Balance of Antarctica, Annals of Glaciology, 14, 78–84, https://doi.org/10.3189/S0260305500008302, 1990.

Fretwell, P., Pritchard, H. D., Vaughan, D. G., Bamber, J. L., Barrand, N. E., Bell, R., Bianchi, C., Bingham, R. G., Blankenship, D. D., Casassa, G., Catania, G., Callens, D., Conway, H., Cook, A. J., Corr, H. F. J., Damaske, D., Damm, V., Ferraccioli, F., Forsberg, R., Fujita, S., Gim, Y., Gogineni, P., Griggs, J. A., Hindmarsh, R. C. A., Holmlund, P., Holt, J. W., Jacobel, R. W., Jenkins, A., Jokat, W., Jordan, T., King, E. C., Kohler, J., Krabill, W., Riger-Kusk, M., Langley, K. A., Leitchenkov, G., Leuschen, C., Luyendyk, B. P., Matsuoka, K., Mouginot, J., Nitsche, F. O., Nogi, Y., Nost, O. A., Popov, S. V., Rignot, E., Rippin, D. M., Rivera, A., Roberts, J., Ross, N., Siegert, M. J., Smith, A. M., Steinhage, D., Studinger, M., Sun, B., Tinto, B. K., Welch, B. C., Wilson, D., Young, D. A., Xiangbin, C., and Zirizzotti, A.: Bedmap2: improved ice bed, surface and thickness datasets for Antarctica, The Cryosphere, 7, 375–393, https://doi.org/10.5194/tc-7-375-2013, 2013.

Frieler, K., Meinshausen, M., Mengel, M., Braun, N., and Hare, W.: A Scaling Approach to Probabilistic Assessment of Regional Climate Change, Journal of Climate, 25, 3117–3144, https://doi.org/10.1175/JCLI-D-11-00199.1, 2012.

https://doi.org/10.5194/esd-2019-78
Preprint. Discussion started: 6 January 2020

Frieler, K., Clark, P. U., He, F., Buizert, C., Reese, R., Ligtenberg, S. R. M., van den Broeke, M. R., Winkelmann, R., and Levermann, A.: Consistent evidence of increasing Antarctic accumulation with warming, Nature Climate Change, 5, 348–352, https://doi.org/10.1038/nclimate2574, 2015.

Fürst, J. J., Durand, G., Gillet-Chaulet, F., Tavard, L., Rankl, M., Braun, M., and Gagliardini, O.: The safety band of Antarctic ice shelves, Nature Climate Change, 6, 479–482, https://doi.org/10.1038/nclimate2912, 2016.

Fyke, J., Lenaerts, J. T. M., and Wang, H.: Basin-scale heterogeneity in Antarctic precipitation and its impact on surface mass variability, The Cryosphere, 11, 2595–2609, https://doi.org/10.5194/tc-11-2595-2017, 2017.

Gill, A.: Atmosphere-ocean dynamics, vol. 30 of *International Geophysics Series*, Academic Press, San Diego, California 92101, 1982.

Golledge, N. R., Kowalewski, D. E., Naish, T. R., Levy, R. H., Fogwill, C. J., and Gasson, E. G. W.: The multi-millennial Antarctic commitment to future sea-level rise, Nature, 526, 421–425, https://doi.org/10.1038/nature15706, 2015.

Gregory, J. and Huybrechts, P.: Ice-sheet contributions to future sea-level change., Philosophical transactions. Series A, Mathematical, physical, and engineering sciences, 364, 1709–31, https://doi.org/10.1098/rsta.2006.1796, 2006.

Haumann, F. A., Gruber, N., Münnich, M., Frenger, I., and Kern, S.: Sea-ice transport driving Southern Ocean salinity and its recent trends, Nature, 537, 89–92, https://doi.org/10.1038/nature19101, 2016.

Held, I. M. and Soden, B. J.: Robust Responses of the Hydrological Cycle to Global Warming, Journal of Climate, 19, 5686–5699, https://doi.org/10.1175/JCLI3990.1, 2006.

Hellmer, H. H., Kauker, F., Timmermann, R., Determann, J., and Rae, J.: Twenty-first-century warming of a large Antarctic ice-shelf cavity by a redirected coastal current, Nature, 485, 225–228, https://doi.org/10.1038/nature11064, 2012.

Heuzé, C., Heywood, K. J., Stevens, D. P., and Ridley, J. K.: Southern Ocean bottom water characteristics in CMIP5 models, Geophysical Research Letters, 40, 1409–1414, https://doi.org/10.1002/grl.50287, 2013.

Hock, R.: Glacier melt: a review of processes and their modelling, Progress in Physical Geography, 29, 362–391, https://doi.org/10.1191/0309133305pp453ra, 2005.

Hughes, T., Zhao, Z., Hintz, R., and Fastook, J.: Instability of the Antarctic Ross Sea Embayment as climate warms, Reviews of Geophysics, pp. 1–36, https://doi.org/10.1002/2016RG000545, 2017.

Jacobs, S.: Observations of change in the Southern Ocean., Philosophical transactions. Series A, Mathematical, physical, and engineering sciences, 364, 1657–81, https://doi.org/10.1098/rsta.2006.1794, 2006.

Jeong, S., Howat, I. M., and Bassis, J. N.: Accelerated ice shelf rifting and retreat at Pine Island Glacier, West Antarctica, Geophysical Research Letters, 43, 11 720–11 725, https://doi.org/10.1002/2016GL071360, 2016.

Kingslake, J., Ely, J. C., Das, I., and Bell, R. E.: Widespread movement of meltwater onto and across Antarctic ice shelves, Nature, 544, 349–352, https://doi.org/10.1038/nature22049, 2017.

Knutti, R., Masson, D., and Gettelman, A.: Climate model genealogy: Generation CMIP5 and how we got there, Geophysical Research Letters, 40, 1194–1199, https://doi.org/10.1002/grl.50256, 2013.

Krinner, G., Largeron, C., Ménégoz, M., Agosta, C., and Brutel-Vuilmet, C.: Oceanic Forcing of Antarctic Climate Change: A Study Using a Stretched-Grid Atmospheric General Circulation Model, Journal of Climate, 27, 5786–5800, https://doi.org/10.1175/JCLI-D-13-00367.1, 2014.

Leclercq, P., Oerlemans, J., and Cogley, J.: Estimating the Glacier Contribution to Sea-Level Rise for the Period 1800–2005, Surveys in Geophysics, 32, 519–535, https://doi.org/10.1007/s10712-011-9121-7, 2011.

https://doi.org/10.5194/esd-2019-78
Preprint. Discussion started: 6 January 2020

Levermann, A., Albrecht, T., Winkelmann, R., Martin, M., Haseloff, M., and Joughin, I.: Kinematic first-order calving law implies potential for abrupt ice-shelf retreat, The Cryosphere, 6, 273–286, https://doi.org/10.5194/tc-6-273-2012, 2012.

Li, G., Harrison, S. P., Bartlein, P. J., Izumi, K., and Colin Prentice, I.: Precipitation scaling with temperature in warm and cold climates: An analysis of CMIP5 simulations, Geophysical Research Letters, 40, 4018–4024, https://doi.org/10.1002/grl.50730, 2013.

Lingle, C. S. and Clark, J. A.: A numerical model of interactions between a marine ice sheet and the solid earth: Application to a West Antarctic ice stream, Journal of Geophysical Research, 90, 1100–1114, https://doi.org/10.1029/JC090iC01p01100, 1985.

Liu, J.: Interpretation of recent Antarctic sea ice variability, Geophysical Research Letters, 31, 2000–2003, https://doi.org/10.1029/2003GL018732, 2004.

Liu, Y., Moore, J. C., Cheng, X., Gladstone, R. M., Bassis, J. N., Liu, H., Wen, J., and Hui, F.: Ocean-driven thinning enhances iceberg calving and retreat of Antarctic ice shelves, Proceedings of the National Academy of Sciences, 112, 3263–3268, https://doi.org/10.1073/pnas.1415137112, 2015.

Locarnini, R. A., Mishonov, A. V., Antonov, T. P., Boyer, T., and Garcia, H.: World Ocean Atlas 2009, Volume 1: Temperature, Tech. rep., NOAA Atlas NESDIS 68, U.S. Government Printing Office, Washington, D.C., https://www.nodc.noaa.gov/OC5/WOA09/pr{_}woa09.html, 2010.

Marshall, G. J., Thompson, D. W. J., and Broeke, M. R.: The Signature of Southern Hemisphere Atmospheric Circulation Patterns in Antarctic Precipitation, Geophysical Research Letters, 44, 11,580–11,589, https://doi.org/10.1002/2017GL075998, 2017.

Meijers, A. J. S.: The Southern Ocean in the Coupled Model Intercomparison Project phase 5, Philosophical Transactions of the Royal Society A: Mathematical, Physical and Engineering Sciences, 372, 20130 296–20130 296, https://doi.org/10.1098/rsta.2013.0296, 2014.

Mengel, M. and Levermann, A.: Ice plug prevents irreversible discharge from East Antarctica, Nature Climate Change, pp. 1–5, https://doi.org/10.1038/nclimate2226, 2014.

Mengel, M., Feldmann, J., and Levermann, A.: Linear sea-level response to abrupt ocean warming of major West Antarctic ice basin, Nature Climate Change, 6, 71–74, https://doi.org/10.1038/nclimate2808, 2015.

Milillo, P., Rignot, E., Rizzoli, P., Scheuchl, B., Mouginot, J., Bueso-Bello, J., and Prats-Iraola, P.: Heterogeneous retreat and ice melt of Thwaites Glacier, West Antarctica, Science Advances, 5, eaau3433, 8pp, https://doi.org/10.1126/sciadv.aau3433, 2019.

Morris, E. M. and Vaughan, D. G.: Spatial and temporal variation of surface temperature on the Antarctic Peninsula and the limit of viability of ice shelves, in: Antarctic Peninsula Climate Variability: Historical and Paleoenvironmental Perspectives, edited by Domack, E., Levente, A., Burnet, A., Bindschadler, R. ., Convey, P., and Kirby, M., vol. 79 of *Antarctic Research Series*, pp. 61–68, American Geophysical Union, Washington, D.C., https://doi.org/10.1029/AR079p0061, 2003.

Moss, R. H., Edmonds, J. A., Hibbard, K. A., Manning, M. R., Rose, S. K., van Vuuren, D. P., Carter, T. R., Emori, S., Kainuma, M., Kram, T., Meehl, G. A., Mitchell, J. F., Nakicenovic, N., Riahi, K., Smith, S. J., Stouffer, R. J., Thomson, A. M., Weyant, J. P., and Wilbanks, T. J.: The next generation of scenarios for climate change research and assessment., Nature, 463, 747–56, https://doi.org/10.1038/nature08823, http://www.nature.com/nature/journal/v463/n7282/full/nature08823.html, 2010.

Mulvaney, R., Abram, N. J., Hindmarsh, R. C., Arrowsmith, C., Fleet, L., Triest, J., Sime, L. C., Alemany, O., and Foord, S.: Recent Antarctic Peninsula warming relative to Holocene climate and ice-shelf history., Nature, 489, 141–144, https://doi.org/10.1038/nature11391, http://www.ncbi.nlm.nih.gov/pubmed/22914090, 2012.

Naughten, K. A., Meissner, K. J., Galton-Fenzi, B. K., England, M. H., Timmermann, R., and Hellmer, H. H.: Future Projections of Antarctic Ice Shelf Melting Based on CMIP5 Scenarios, Journal of Climate, 31, 5243–5261, https://doi.org/10.1175/JCLI-D-17-0854.1, http://journals.ametsoc.org/doi/10.1175/JCLI-D-17-0854.1, 2018.

https://doi.org/10.5194/esd-2019-78
Preprint. Discussion started: 6 January 2020

Nicholls, K. W., Østerhus, S., Makinson, K., Gammelsrød, T., and Fahrbach, E.: Ice-ocean processes over the continental shelf of the southern Weddell Sea, Antarctica: A review, Reviews of Geophysics, 47, 23pp, https://doi.org/10.1029/2007RG000250, http://www.agu.org/pubs/crossref/2009/2007RG000250.shtml, 2009.

Ohmura, A.: Physical Basis for the Temperature-Based Melt-Index Method, Journal of Applied Meteorology, 40, 753–761, https://doi.org/10.1175/1520-0450(2001)040<0753:PBFTTB>2.0.CO;2, http://journals.ametsoc.org/doi/abs/10.1175/1520-0450(2001)040{%}3C0753:PBFTTB{%}3E2.0.CO;2, 2001.

Palerme, C., Genthon, C., Claud, C., Kay, J. E., Wood, N. B., and L'Ecuyer, T.: Evaluation of current and projected Antarctic precipitation in CMIP5 models, Climate Dynamics, 48, 225–239, https://doi.org/10.1007/s00382-016-3071-1, 2017.

Paolo, F. S., Padman, L., Fricker, H. A., Adusumilli, S., Howard, S., and Siegfried, M. R.: Response of Pacific-sector Antarctic ice shelves to the El Niño/Southern Oscillation, Nature Geoscience, 11, 121–126, https://doi.org/10.1038/s41561-017-0033-0, http://www.nature.com/articles/s41561-017-0033-0, 2018.

Pollard, D. and DeConto, R. M.: Modelling West Antarctic ice sheet growth and collapse through the past five million years., Nature, 458, 329–32, https://doi.org/10.1038/nature07809, http://www.ncbi.nlm.nih.gov/pubmed/19295608, 2009.

Pollard, D., Deconto, R. M., and Alley, R. B.: Potential Antarctic Ice Sheet retreat driven by hydrofracturing and ice cliff failure, Earth and Planetary Science Letters, 412, 112–121, https://doi.org/10.1016/j.epsl.2014.12.035, http://dx.doi.org/10.1016/j.epsl.2014.12.035, 2015.

Rignot, E., Jacobs, S., Mouginot, J., and Scheuchl, B.: Ice-Shelf Melting Around Antarctica, Science, 341, 266–270, https://doi.org/10.1126/science.1235798, http://www.sciencemag.org/cgi/doi/10.1126/science.1235798, 2013.

Rignot, E., Mouginot, J., Morlighem, M., Seroussi, H., and Scheuchl, B.: Widespread, rapid grounding line retreat of Pine Island, Thwaites, Smith, and Kohler glaciers, West Antarctica, from 1992 to 2011, Geophysical Research Letters, 41, 3502–3509, https://doi.org/10.1002/2014GL060140, http://doi.wiley.com/10.1002/2014GL060140, 2014.

Rignot, E., Mouginot, J., and Scheuchl, B.: MEaSUREs Antarctic Grounding Line from Differential Satellite Radar Interferometry, Version 2., Boulder, Colorado USA. NASA National Snow and Ice Data Center Distributed Active Archive Center, https://doi.org/10.5067/IKBWW4RYHF1Q, last Accessed: 16. Aug. 2018, 2016.

Ritz, C., Edwards, T. L., Durand, G., Payne, A. J., Peyaud, V., and Hindmarsh, R. C. A.: Potential sea-level rise from Antarctic ice-sheet instability constrained by observations, Nature, 528, 115–118, https://doi.org/10.1038/nature16147, http://dx.doi.org/10.1038/nature16147, 2015.

Rott, H., Skvarca, P., and Nagler, T.: Rapid Collapse of Northern Larsen Ice Shelf, Antarctica, Science, 271, 788–792, https://doi.org/10.1126/science.271.5250.788, http://www.sciencemag.org/cgi/doi/10.1126/science.271.5250.788, 1996.

Rott, H., Müller, F., Nagler, T., and Floricioiu, D.: The imbalance of glaciers after disintegration of Larsen-B ice shelf, Antarctic Peninsula, The Cryosphere, 5, 125–134, https://doi.org/10.5194/tc-5-125-2011, http://www.the-cryosphere.net/5/125/2011/, 2011.

Sallée, J.-B., Shuckburgh, E., Bruneau, N., Meijers, A., Bracegirdle, T., and Wang, Z.: Assessment of Southern Ocean mixed-layer depths in CMIP5 models: Historical bias and forcing response, Journal of Geophysical Research: Oceans, 118, 18pp, https://doi.org/10.1002/jgrc.20157, http://doi.wiley.com/10.1002/jgrc.20157, 2013a.

Sallée, J.-B., Shuckburgh, E., Bruneau, N., Meijers, A., Bracegirdle, T., Wang, Z., and Roy, T.: Assessment of Southern Ocean water mass circulation and characteristics in CMIP5 models: Historical bias and forcing response, Journal of Geophysical Research: Oceans, 118, 1830–1844, https://doi.org/10.1002/jgrc.20135, http://doi.wiley.com/10.1002/jgrc.20135, 2013b.

Sasgen, I., Konrad, H., Helm, V., and Grosfeld, K.: High-Resolution Mass Trends of the Antarctic Ice Sheet through a Spectral Combination of Satellite Gravimetry and Radar Altimetry Observations, Remote Sensing, 11, 144, https://doi.org/10.3390/rs11020144, 2019.

https://doi.org/10.5194/esd-2019-78
Preprint. Discussion started: 6 January 2020

Scambos, T. A., Bell, R. E., Alley, R. B., Anandakrishnan, S., Bromwich, D. H., Brunt, K., Christianson, K., Creyts, T., Das, S. B., DeConto, R., Dutrieux, P., Fricker, H. A., Holland, D., MacGregor, J., Medley, B., Nicolas, J. P., Pollard, D., Siegfried, M. R., Smith, A. M., Steig, E. J., Trusel, L. D., Vaughan, D. G., and Yager, P. L.: How much, how fast?: A science review and outlook for research on the instability of Antarctica's Thwaites Glacier in the 21st century, Global and Planetary Change, 153, 16–34, https://doi.org/10.1016/j.gloplacha.2017.04.008, http://dx.doi.org/10.1016/j.gloplacha.2017.04.008, 2017.

Schoof, C.: A variational approach to ice stream flow, Journal of Fluid Mechanics, 556, 227–251, https://doi.org/10.1017/S0022112006009591, http://www.journals.cambridge.org/abstract{_}S0022112006009591, 2006.

Seroussi, H., Nowicki, S., Simon, E., Abe-Ouchi, A., Albrecht, T., Brondex, J., Cornford, S., Dumas, C., Gillet-Chaulet, F., Goelzer, H., Golledge, N. R., Gregory, J. M., Greve, R., Hoffman, M. J., Humbert, A., Huybrechts, P., Kleiner, T., Larour, E., Leguy, G., Lipscomb, W. H., Lowry, D., Mengel, M., Morlighem, M., Pattyn, F., Payne, A. J., Pollard, D., Price, S. F., Quiquet, A., Reerink, T. J., Reese, R., Rodehacke, C. B., Schlegel, N.-J., Shepherd, A., Sun, S., Sutter, J., Van Breedam, J., van de Wal, R. S. W., Winkelmann, R., and Zhang, T.: initMIP-Antarctica: an ice sheet model initialization experiment of ISMIP6, The Cryosphere, 13, 1441–1471, https://doi.org/10.5194/tc-13-1441-2019, https://www.the-cryosphere.net/13/1441/2019/, 2019a.

Seroussi, H., Nowicki, S., Simon, E., and ISMIP6: ISMIP6 Antarctic Projections: Parameterization of Climate Forcings and First Results, https://www.czech-in.org/cmPortalV15/CM_W3_Searchable/iugg19/normal#!abstractdetails/0000739190, 2019b.

Shepherd, A., Ivins, E., Geruo, A., Barletta, V., Bentley, M., Bettadpur, S., Briggs, K., Bromwich, D., Forsberg, R., Galin, N., Horwath, M., Jacobs, S., Joughin, I., King, M., Lenaerts, J., Li, J., Ligtenberg, S., Luckman, A., Luthcke, S., McMillan, M., Meister, R., Milne, G., Mouginot, J., Muir, A., Nicolas, J., Paden, J., Payne, A., Pritchard, H., Rignot, E., Rott, H., Sorensen, L., Scambos, T., Scheuchl, B., Schrama, E., Smith, B., Sundal, A., van Angelen, J., van de Berg, W., van den Broeke, M., Vaughan, D., Velicogna, I., Wahr, J., Whitehouse, P., Wingham, D., Yi, D., Young, D., and Zwally, H.: A Reconciled Estimate of Ice-Sheet Mass Balance, Science, 338, 1183–1189, https://doi.org/10.1126/science.1228102, http://www.sciencemag.org/cgi/doi/10.1126/science.1228102, 2012.

Sun, Y., Solomon, S., Dai, A., and Portmann, R. W.: How Often Will It Rain?, Journal of Climate, 20, 4801–4818, https://doi.org/10.1175/JCLI4263.1, http://journals.ametsoc.org/doi/abs/10.1175/JCLI4263.1, 2007.

Sutter, J., Fischer, H., Grosfeld, K., Karlsson, N. B., Kleiner, T., Liefferinge, B. V., and Eisen, O.: Modelling the Antarctic Ice Sheet across the mid-Pleistocene transition – implications for Oldest Ice, The Cryosphere, 13, 2023–2041, https://doi.org/10.5194/tc-13-2023-2019, 2019.

Thomas, E., Dennis, P., Bracegirdle, T., and Franzke, C.: Ice core evidence for significant 100-year regional warming on the Antarctic Peninsula, Geophysical Research Letters, 36, 5pp, https://doi.org/10.1029/2009GL040104, http://www.agu.org/pubs/crossref/2009/2009GL040104.shtml, 2009.

Thomas, E. R., van Wessem, J. M., Roberts, J., Isaksson, E., Schlosser, E., Fudge, T. J., Vallelonga, P., Medley, B., Lenaerts, J., Bertler, N., van den Broeke, M. R., Dixon, D. A., Frezzotti, M., Stenni, B., Curran, M., and Ekaykin, A. A.: Regional Antarctic snow accumulation over the past 1000 years, Climate of the Past, 13, 1491–1513, https://doi.org/10.5194/cp-13-1491-2017, https://www.clim-past.net/13/1491/2017/, 2017.

Turner, J., Bracegirdle, T. J., Phillips, T., Marshall, G. J., and Hosking, J. S.: An Initial Assessment of Antarctic Sea Ice Extent in the CMIP5 Models, Journal of Climate, 26, 1473–1484, https://doi.org/10.1175/JCLI-D-12-00068.1, http://journals.ametsoc.org/doi/10.1175/JCLI-D-12-00068.1, 2013.

van den Broeke, M.: Strong surface melting preceded collapse of Antarctic Peninsula ice shelf, Geophysical Research Letters, 32, 4pp, https://doi.org/10.1029/2005GL023247, http://doi.wiley.com/10.1029/2005GL023247, 2005.

https://doi.org/10.5194/esd-2019-78
Preprint. Discussion started: 6 January 2020

Van Wessem, J., Reijmer, C., Morlighem, M., Mouginot, J., Rignot, E., Medley, B., Joughin, I., Wouters, B., Depoorter, M., Bamber, J., Lenaerts, J., Van De Berg, W., Van Den Broeke, M., and Van Meijgaard, E.: Improved representation of East Antarctic surface mass balance in a regional atmospheric climate model, Journal of Glaciology, 60, 761–770, https://doi.org/10.3189/2014JoG14J051, https://www.cambridge.org/core/product/identifier/S0022143000203110/type/journal{_}article, 2014.

Wang, Y., Ding, M., van Wessem, J. M., Schlosser, E., Altnau, S., van den Broeke, M. R., Lenaerts, J. T. M., Thomas, E. R., Isaksson, E., Wang, J., and Sun, W.: A Comparison of Antarctic Ice Sheet Surface Mass Balance from Atmospheric Climate Models and In Situ Observations, Journal of Climate, 29, 5317–5337, https://doi.org/10.1175/JCLI-D-15-0642.1, 2016.

Wang, Y., Thomas, E. R., Hou, S., Huai, B., Wu, S., Sun, W., Qi, S., Ding, M., and Zhang, Y.: Snow Accumulation Variability Over the West Antarctic Ice Sheet Since 1900: A Comparison of Ice Core Records With ERA-20C Reanalysis, Geophysical Research Letters, pp. 1–9, https://doi.org/10.1002/2017GL075135, 2017.

Wingham, D. J., Shepherd, A., Muir, A., and Marshall, G. J.: Mass balance of the Antarctic Ice Sheet from 1992 to 2017, Nature, 558, 219–222, https://doi.org/10.1038/s41586-018-0179-y, 2018.

Winkelmann, R., Martin, M., Haseloff, M., Albrecht, T., Bueler, E., Khroulev, C., and Levermann, A.: The Potsdam Parallel Ice Sheet Model (PISM-PIK) – Part 1: Model description, The Cryosphere, 5, 715–726, https://doi.org/10.5194/tc-5-715-2011, 2011.

Winkelmann, R., Levermann, A., Martin, M., and Frieler, K.: Increased future ice discharge from Antarctica owing to higher snowfall, Nature, 492, 239–242, https://doi.org/10.1038/nature11616, 2012.

Winkelmann, R., Levermann, A., Ridgwell, A., and Caldeira, K.: Combustion of available fossil fuel resources sufficient to eliminate the Antarctic Ice Sheet, Science Advances, 1, e1500 589, 5pp, https://doi.org/10.1126/sciadv.1500589, 2015.

Yin, J., Gentine, P., Zhou, S., Sullivan, S. C., Wang, R., Zhang, Y., and Guo, S.: Large increase in global storm runoff extremes driven by climate and anthropogenic changes, Nature Communications, 9, 4389, 10pp, https://doi.org/10.1038/s41467-018-06765-2, 2018.

https://doi.org/10.5194/esd-2019-78
Preprint. Discussion started: 6 January 2020

Earth System Dynamics Discussions
Open Access
EGU

Tables

Table 1. List of CMIP5 models and the used RCP climate projections (Moss et al., 2010) beside historical (hist) piControl (piCtrl) scenarios. Please note that we do not use the RCP2.6 scenario of the CCSM4 model.

Model Name	RCP Projections	Scenarios
CanESM2	RCP2.6, RCP4.5, RCP8.5	hist, piCtrl
CCSM4	RCP4.5, RCP8.5	hist, piCtrl
CNRM-CM5	RCP2.6, RCP4.5, RCP8.5	hist, piCtrl
CSIRO-Mk3.6.0	RCP2.6, RCP4.5, RCP8.5	hist, piCtrl
HadGEM2-ES	RCP2.6, RCP4.5, RCP8.5	hist, piCtrl
MIROC-ESM	RCP2.6, RCP4.5, RCP8.5	hist, piCtrl
MPI-ESM-LR	RCP2.6, RCP4.5, RCP8.5	hist, piCtrl
MRI-CGCM3	RCP2.6, RCP4.5, RCP8.5	hist, piCtrl
NorESM1-M	RCP2.6, RCP4.5, RCP8.5	hist, piCtrl

https://doi.org/10.5194/esd-2019-78
Preprint. Discussion started: 6 January 2020

Earth System Dynamics
Discussions
Open Access
EGU

Table 2. Forcing used for ice-sheet model spin-up and as reference fields for the anomaly forcing.

Forcing	Period	Label	Reference Fields	Reference
Atmosphere	1979–2011	RACMO 2.3/ANT	2m-air temperature, Total precipitation	Van Wessem et al. (2014)
Ocean	Climatological mean	World Ocean Atlas 2009 (WOA09)	Potential ocean temperature	Locarnini et al. (2010)

https://doi.org/10.5194/esd-2019-78
Preprint. Discussion started: 6 January 2020

Earth System Dynamics
Discussions
Open Access
EGU

Table 3. Temperature scaling of the precipitation for six ice core locations in Antarctica. The second column lists the ensemble mean scaling (RCP8.5, first 50 years, both initial states PISM1Eq and PISM2Eq) and standard deviation (2-sigma) across all ensemble members. The third column provides scaling factors deduced from ice cores (Frieler et al., 2015), including the provided error margins (2-sigma). Please inspect Figure 4 for the ice core locations.

Core Name Location	Scaling of Ensemble Mean	Scaling Ice Core
EDML	11.0±6.6	5.0±2.8
Vostok	14.0±5.6	6.1±2.5
Law Dome	5.8±6.3	5.2±2.3
EDC	11.0±5.0	5.9±2.2
Talos Dome	8.4±5.2	6.8±2.8
WAIS	6.8±5.4	5.5±1.2

https://doi.org/10.5194/esd-2019-78
Preprint. Discussion started: 6 January 2020

Earth System Dynamics
Discussions
Open Access
EGU

Table 4. Defined areas as part of our diagnostic. The fraction is computed relative to "glaciered." Figure 4 and Figure 5 depict these areas.

Region Label	Area (10^6 km^2)	Fraction (%)	Longitude Range	Comment
glaciered	13.6	100.0	$[-180°\mathrm{E}, +180°\mathrm{E}[$	Antarctica incl. ice shelves
grounded	11.9	87.5	$[-180°\mathrm{E}, +180°\mathrm{E}[$	Without ice shelves
EAIS Atl	3.77	27.6	$[-45°\mathrm{E}, +55°\mathrm{E}]$	Including floating ice shelves
EAIS Ind	5.66	41.1	$[+55°\mathrm{E}, +155°\mathrm{E}]$	
WAIS	4.26	31.3	$[+155°\mathrm{E}, -45°\mathrm{E}]$	
Siple Coast	0.69	5.12	$[+155°\mathrm{E}, -140°\mathrm{E}]$	Latitude$> 85°$S

https://doi.org/10.5194/esd-2019-78
Preprint. Discussion started: 6 January 2020

Earth System Dynamics
Discussions
Open Access
EGU

850 **Figures**

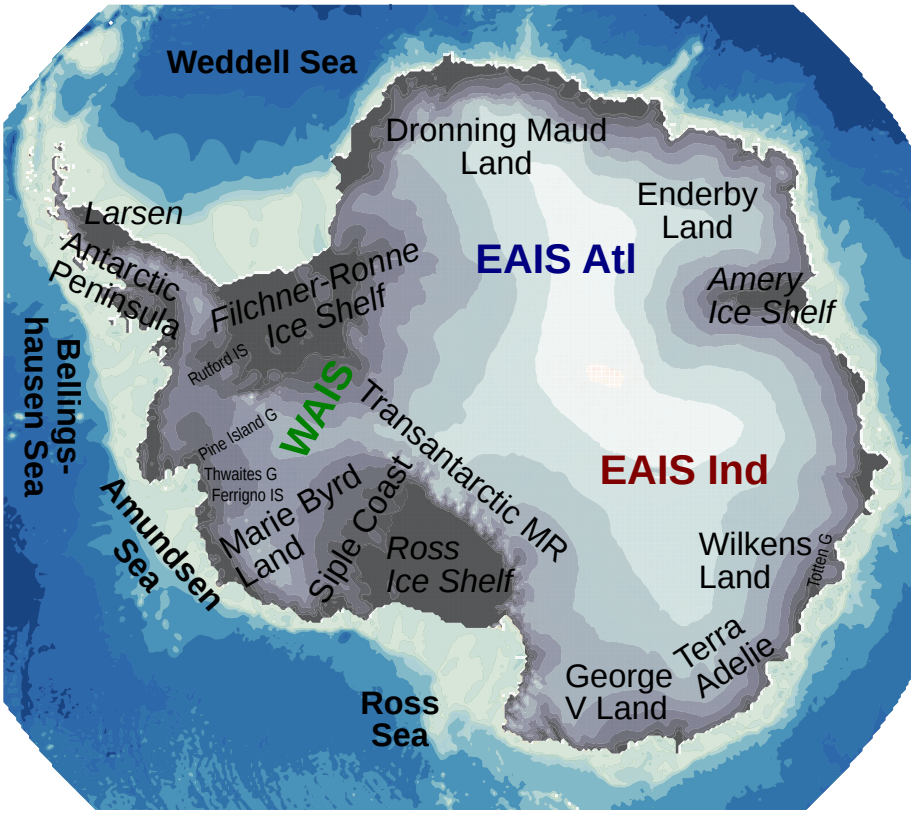

Figure 1. Map of Antarctica. The seafloor depth is shown with a blue color scale, while the elevation of Antarctica above sea level is depicted by a colorbar of dark-grey (low elevation) to white colors (high elevation). The font style of ocean labels is in bold and of ice shelves is in italic. The smaller font size tags individual glacier (G) and ice streams (IS). The abbreviation "MR" stands for "Mountain Range". Colored labels define three regions: WAIS: West Antarctic Ice Sheet, EAIS Atl: East Antarctic Ice - Sheet Atlantic Sector, EAIS Ind: East Antarctic Ice Sheet - Indian Ocean Sector. The Figures 4 and 5 show the boundaries of these regions. The here depicted bedrock topography and surface orography are taken from Fretwell et al. (2013).

https://doi.org/10.5194/esd-2019-78
Preprint. Discussion started: 6 January 2020

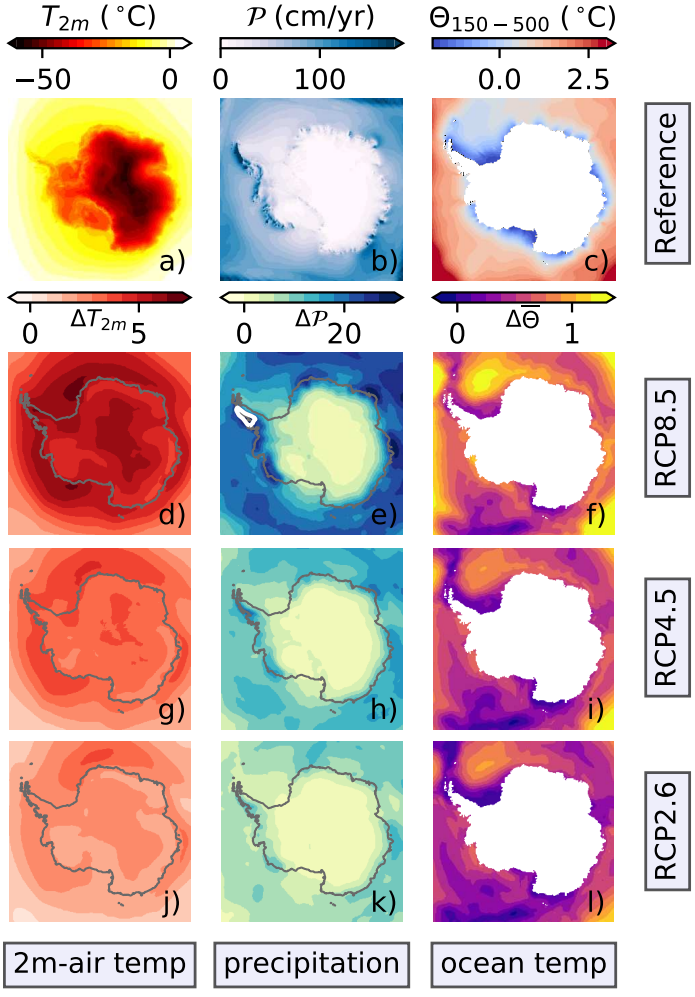

Figure 2. Atmospheric (a, b) and oceanographic (c) reference forcing; ensemble mean anomalies (d–l). The top row represents the reference fields to spin-up the ice-sheet model (Table 2). The 2m-air temperature (a) and the total precipitation (b) are mean fields from the regional RACMO model, while the ocean temperatures come from the World Ocean Atlas 2009 (c); see Table 2 for more details. Each reference field has its colorbar above its plot. Below each reference field, the related anomalies, including their colorbar, are compiled for the period 2071–2100. Here, the second (third and fourth) row shows the anomalies for RCP8.5 (RCP4.5, RCP2.6). In these atmospheric anomaly plots, the dark-gray line follows the current coastline. All potential ocean temperatures (c, f, i, l) are a vertical mean of the depth interval from 150 m to 500 m. The white contour lines in the anomaly plots highlight the following precipitation threshold (e, h, k): 30 cm/yr. All these anomalies are the ensemble mean of the models listed in Table 1; please note that CCSM4 is not part of RCP2.6. Appendix Figure A1 and Figure A2 show the corresponding ensemble maximum and minimum fields, respectively. Antarctica's contours are deduced from Fretwell et al. (2013).

https://doi.org/10.5194/esd-2019-78
Preprint. Discussion started: 6 January 2020

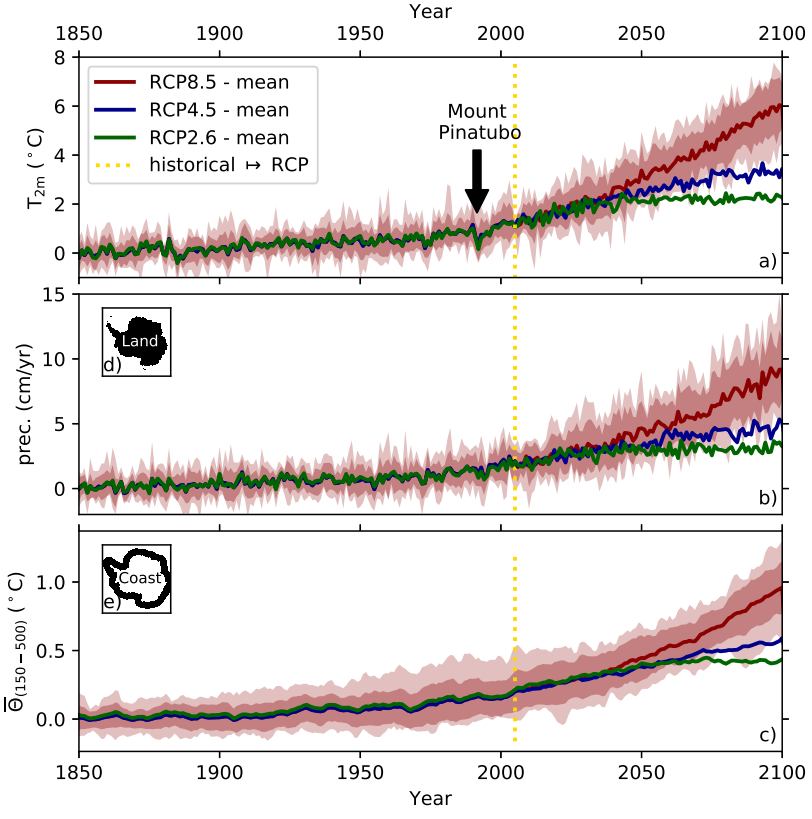

Figure 3. Spatial mean of the a) 2m-air temperature and b) total precipitation anomalies on Antarctica (d). Spatial c) potential ocean temperature mean averaged over the depth interval from 150 m to 500 m in the coastal zone (e) surrounding Antarctica. The ensemble mean values are shown for the scenarios according to the legend in a). The dark red band highlights the 1-sigma standard deviation (66 %), while the light red band shows the full range covered by all ensemble members for RCP8.5 only. The vertical golden line marks the transition from the historical forcing to the RCP. The distinct temperature jump during the historical period in 1991 marks the Mount Pinatubo volcano eruption. The contours of the Antarctic continent (d) follow the outer edges defined by the data set of Fretwell et al. (2013), while the coastal strip (e) is an extension into the sea with smoothed northern edges.

https://doi.org/10.5194/esd-2019-78
Preprint. Discussion started: 6 January 2020

Earth System Dynamics
Discussions
Open Access
EGU

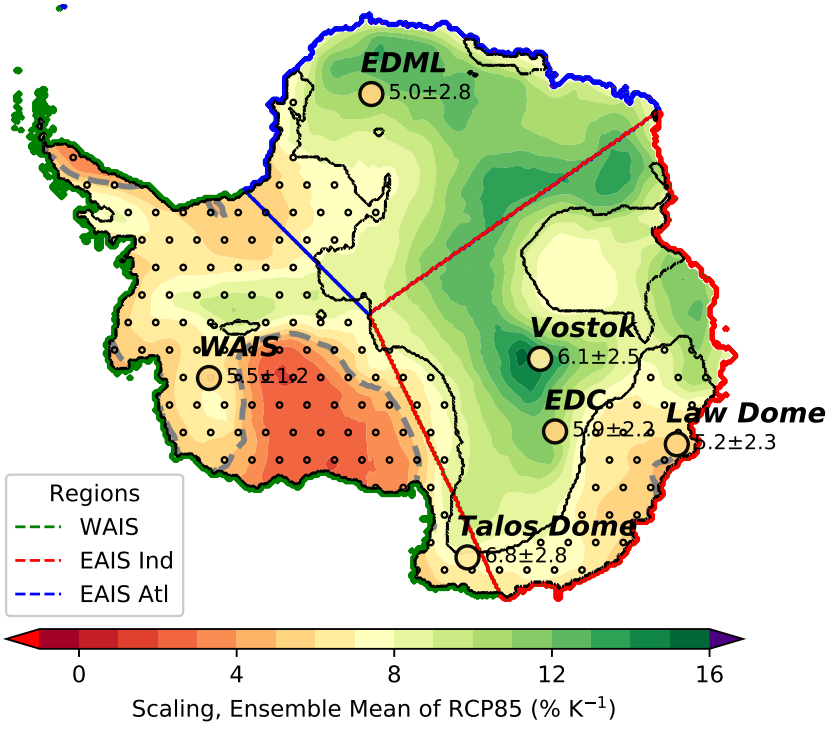

Figure 4. Ensemble mean of the temperature scaled precipitation for the period 2051–2100. This scaling under the RCP8.5 scenario comes from nine CMIP5 models (Table 1), which are driven by anomalies relative to the first 50 years of piControl. In the dotted regions enclosed by black contours, the combined simulated scaling and the standard deviation contains the value of $5\,\%\mathrm{K}^{-1}$. Gray dashed lines follow this $5\,\%\mathrm{K}^{-1}$ contour. The scaling values deduced from ice cores are shown at their location (Frieler et al., 2015) by using the same colorbar as the spatial distribution within the circle. The neighboring printed values are the mean and the 2-sigma uncertainty. Three defined regions (Table 4) named "WAIS", "EAIS Atl", and "EAIS Ind" are outlined by their green, blue, and red, respectively, boundaries (lower left legend). For further details, inspect the text, please. Appendix Figure A3 provides corresponding distributions for each climate model ensemble member. Antarctica's contour is deduced from Fretwell et al. (2013).

https://doi.org/10.5194/esd-2019-78
Preprint. Discussion started: 6 January 2020

Earth System Dynamics
Discussions
Open Access
EGU

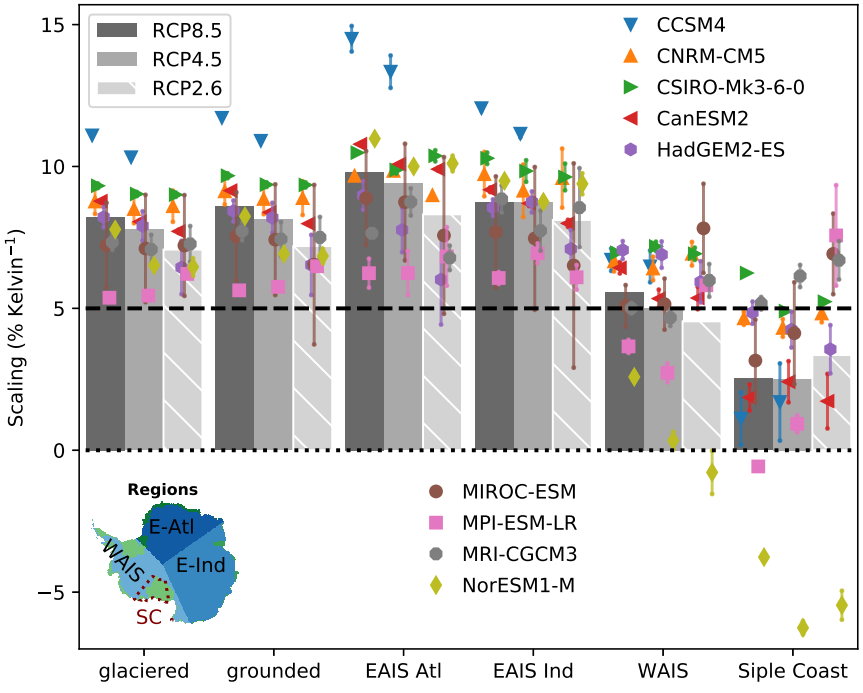

Figure 5. Temperature-precipitation scaling deduced for the nine CMIP5 models (Table 1) and three future scenarios (legend) in six defined regions in Antarctica (see map in the lower-left corner and Table 4. The coastlines and the grounding line positions are deduced from Fretwell et al. (2013)). The gray bars represent the ensemble mean, whereas the individual symbols stand for CMIP5 models. Here the results apply for both reference periods, where the anomalies are computed relative to the first or last 50 years of piControl. Each symbol is the model average of both reference periods, while the attached line indicates the scatter range between the first and last 50 years reference period. Please note, that the RCP2.6 scenario does not include the CCSM4 model; hence, the corresponding bar is hatched.

https://doi.org/10.5194/esd-2019-78
Preprint. Discussion started: 6 January 2020

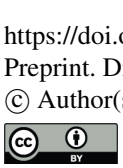

Earth System Dynamics
Discussions
Open Access
EGU

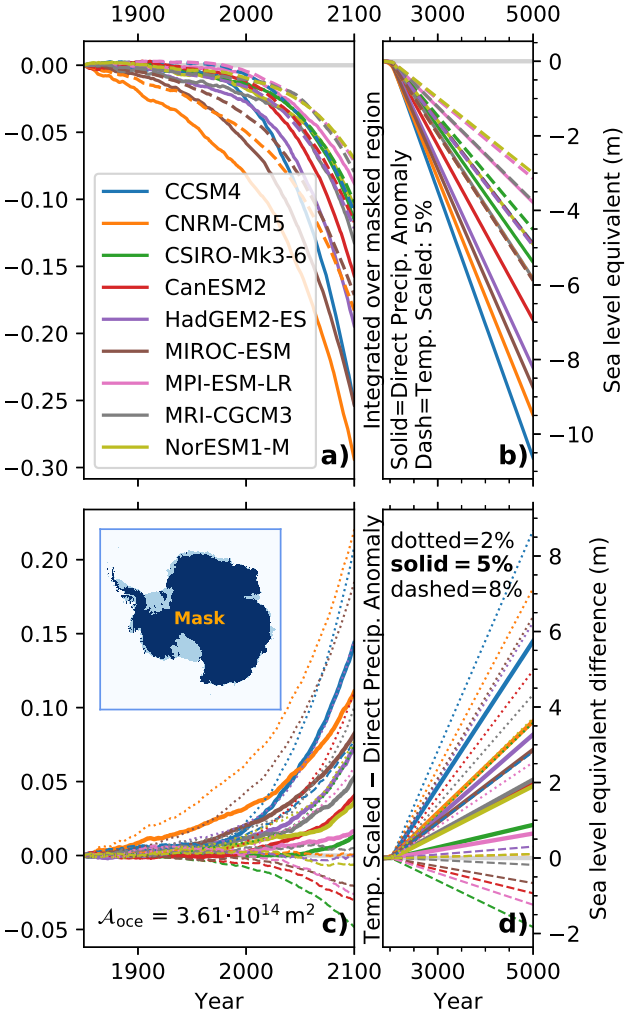

Figure 6. The top row (a, b) shows the integrated sea-level equivalent of the precipitation falling on grounded ice in Antarctica (see dark-blue mask in the lower left, the light-blue parts highlight ice shelves; The grounded and floating ice areas are derived from Fretwell et al. (2013)) for the anomaly forcing (solid lines) and temperature scaled precipitation (dashed lines) considering a scaling of $5\,\%\mathrm{K}^{-1}$. The difference in the sea-level impact between the anomalies and the temperature scaled precipitation is depicted in the lower row (c, d). Here, the solid lines consider scaling of $5\,\%\mathrm{K}^{-1}$, while the dotted and dashed lines consider a scaling of $2\,\%\mathrm{K}^{-1}$ and $8\,\%\mathrm{K}^{-1}$, respectively. The left subfigures a) and c) are restricted to the period 1850-2100, while b) and d) cover the full period from 1850 until 5000. Every single colored line (see legend in the upper left) represents one CMIP5 model (Table 1). The corresponding curves for the scenario RCP4.5 as well as for a different mask that covers the entire continent are available in the Appendix Figure A4.

https://doi.org/10.5194/esd-2019-78
Preprint. Discussion started: 6 January 2020

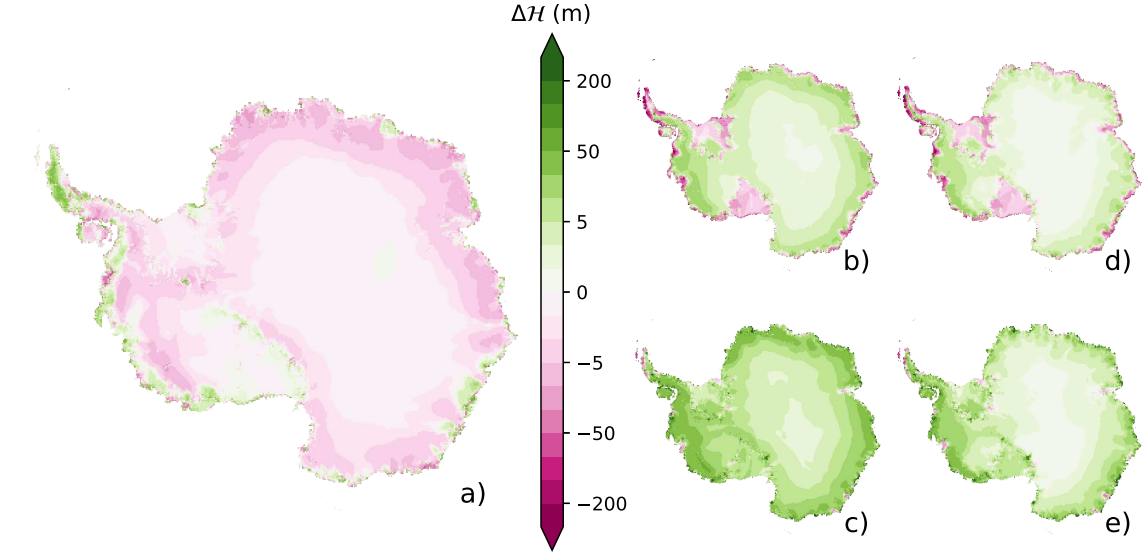

Figure 7. Ice thickness changes under the RCP8.5 scenario in the year 2100 since the year 1850. The ensemble mean difference between the runs forced by the scaled precipitation and the precipitation anomalies (a). For each climate model scenario, the anomalies are computed relative to the 50 years of the related piControl scenario. The simulations driven with the precipitation anomaly (b, c) have the mean ice thickness (b), and the maximum ice thickness (c) changes. The temperature scaled precipitation of $5\,\%\mathrm{K}^{-1}$ gives the corresponding ensemble mean (d) and maximum (e). Please note that all subplots share the same colorbar.

https://doi.org/10.5194/esd-2019-78
Preprint. Discussion started: 6 January 2020

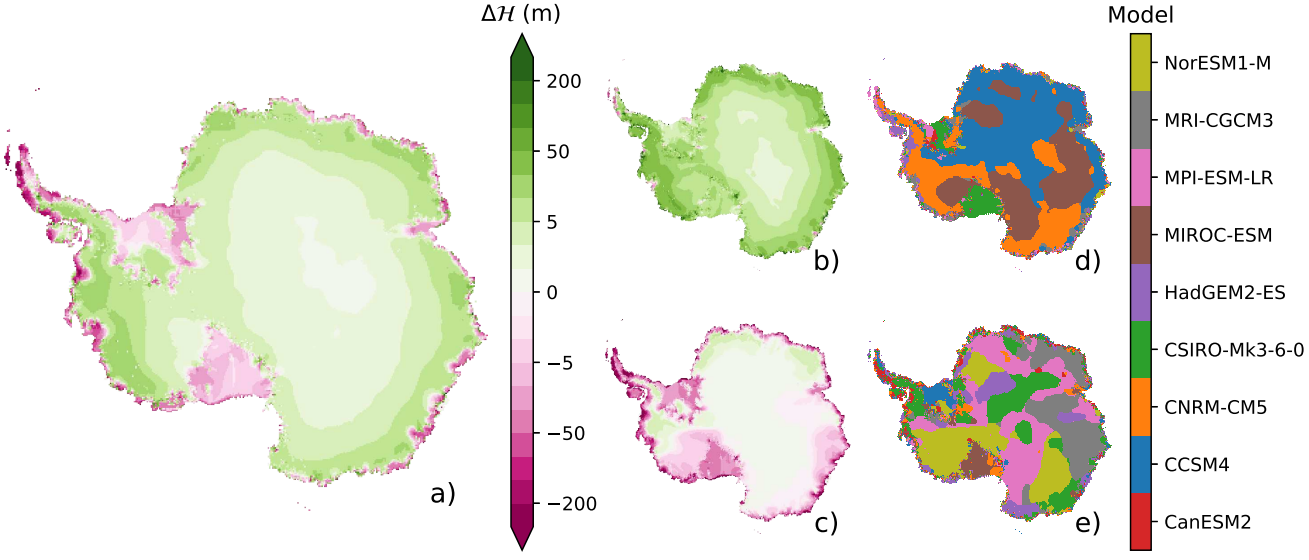

Figure 8. Ice thickness changes since 1850 under the RCP8.5 scenario for the actually applied precipitation anomaly in the year 2100. Highlighted are the (a) ensemble mean, maximum (b), and minimum (c). The climate model that is used to drive the ice-sheet model simulation causing the maximum and minimum thickness are shown in (d) and (e), respectively, next to the ensemble maximum (b) and minimum (c).

https://doi.org/10.5194/esd-2019-78
Preprint. Discussion started: 6 January 2020

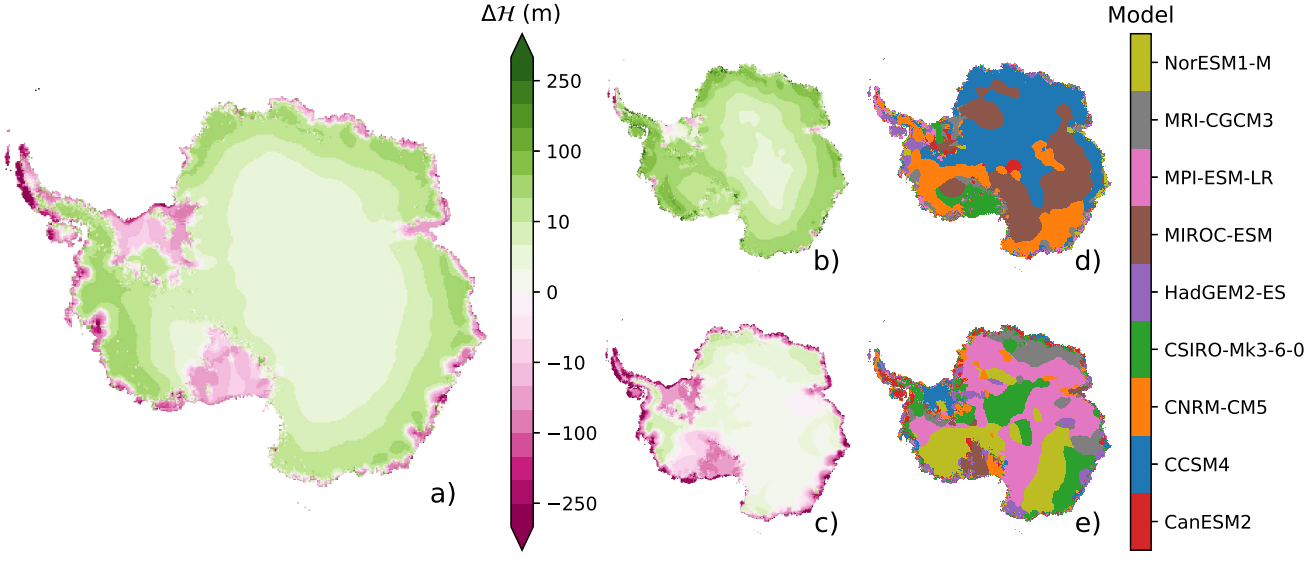

Figure 9. Ice thickness changes since 1850 under the RCP8.5 scenario for applied precipitation anomalies in the year 2200. Highlighted are the (a) ensemble mean, maximum (b), and minimum (c). The climate model that is used to drive the ice-sheet model simulation causing the maximum and minimum thickness are shown in (d) and (e), respectively, next to the ensemble maximum (b) and minimum (c).

https://doi.org/10.5194/esd-2019-78
Preprint. Discussion started: 6 January 2020

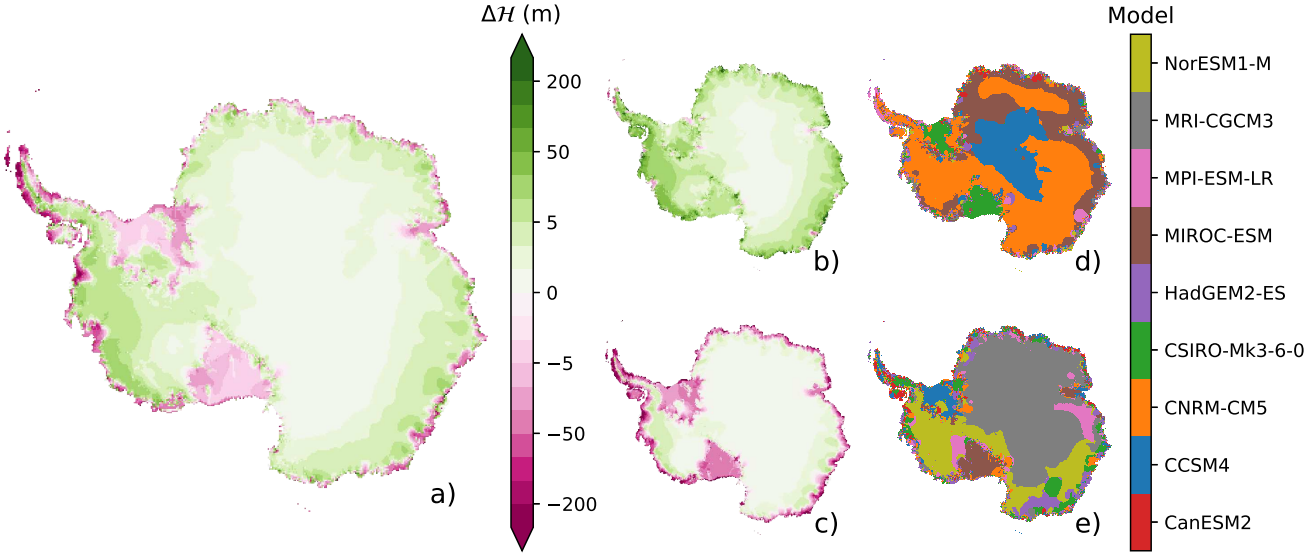

Figure 10. Ice thickness changes since the year 1850 under the RCP8.5 scenario in the model year 2100. Here the precipitation is scaled by the temperature anomaly with a value of $5\,\%\mathrm{K}^{-1}$. Depicted are the (a) ensemble mean, maximum (b), and minimum (c). The climate model that is used to drive the ice-sheet model simulation causing the maximum and minimum thickness is shown in (d) and (e), respectively, next to the ensemble maximum (b) and minimum (c). This figure is similar to Figure 8, but there the results under precipitation anomalies are shown.

https://doi.org/10.5194/esd-2019-78
Preprint. Discussion started: 6 January 2020

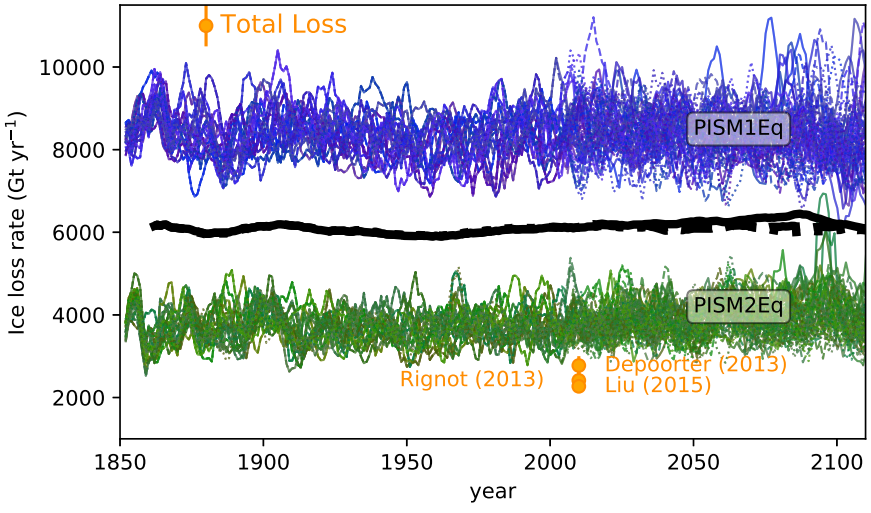

Figure 11. Temporal evolution of the ocean-driven ice loss rates of the fringing ice shelves around Antarctica for the period from 1850 to 2100. The thin blue lines are all ensemble members starting from the initial state PISM1Eq, where the Eigen-calving parameter amounts 10^{18}, while the green lines are the corresponding simulations starting from PISM2Eq (Eigen-calving parameter 10^{17}). A running mean with a window of 5 years has been applied for the thin lines. All simulations start under historical conditions and continue after 2005 under the RCP8.5 (solid lines), RCP4.5 (dashed lines) or RCP2.6 (dotted lines) scenario. The thick black lines represent the ensemble mean of the three future scenarios with a moving window length of 25 years. Recent estimates of the total loss rates (Top-left legend with the golden circles). Estimated uncertainties are given as vertical lines if the uncertainties are larger than the symbol size.

https://doi.org/10.5194/esd-2019-78
Preprint. Discussion started: 6 January 2020

Earth System Dynamics
Discussions
Open Access
EGU

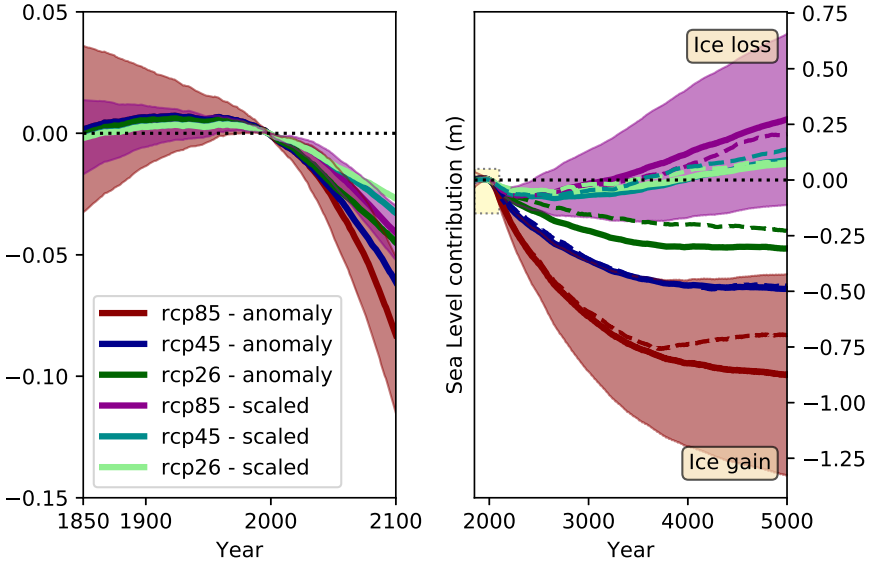

Figure 12. Sea level contribution of Antarctica computed by the ensemble of ice-sheet simulations (please see text for details). The solid lines represent the ensemble averages for the applied precipitation anomalies and the temperature-scaled precipitation boundary conditions according to the legend (lower left), while the dashed lines are the corresponding medians. For the RCP8.5 scenario, the shading highlights the standard deviation (1-sigma) as a measure of the variability among the ice-sheet ensemble members driven by various climate models (Table 1).

https://doi.org/10.5194/esd-2019-78
Preprint. Discussion started: 6 January 2020


Earth System Dynamics Discussions

Appendix A: Additional discussion

Regarding oceanic influence, we focus on the changes of the ensemble mean ocean temperature under the RCP8.5 scenario in a depth range between $150\,\mathrm{m}$ and $500\,\mathrm{m}$ (Figure 3), because the water masses of this range flow into the ice-sheet cavities and are in contact with large parts of ice shelve bases. Highest temperature increases occur in the Bellingshausen and Amundsen Seas as part of the West Antarctic Ice Sheet (WAIS) and some spots along the East Antarctic Ice Sheet (EAIS). In the Bellingshausen and Amundsen Sea warm water masses that flow already into ice-shelf cavities and drive the highest basal melting rates, the potential to trigger Marine Ice Sheet Instability (MISI) exists, because WAIS has a retrograde bedrock topography. The massive ice shelves, Filchner-Ronne, Ross, and Amery, are influenced by moderate temperature increases. However, our setup misses the interaction between the ice-shelf topography and the underlying dynamically evolving ocean. Hence, the setup does not describe related circulation changes that may bring warmer water masses into the ice cavities. For instance, it has been found that warmer water masses could find their way into these ice-shelf cavities and cause a strongly amplified basal mass loss under a changing climate (Hellmer et al., 2012). They have simulated an ocean warming by more then $2\,^{\circ}\mathrm{C}$ in the Filchner Trough (eastern Filchner-Ronne Ice Shelf). At the ice shelves edge of the Filchner-Ronne Ice Shelf, our ensemble maximum ocean temperature anomaly (Figure A1) of about $1.5\,^{\circ}\mathrm{C}$ generates a much weaker forcing.

A1 Temperature Scaling

If one calculates temperature scaling factors out of the CMIP5 model simulated temperature and precipitation changes, it turns out that the temperature scaling factor of the precipitation is different for each model and therefore shows an inhomogeneous spatial pattern (Appendix Figure A3). Furthermore, the details of the scaling factors depend on if we determine the anomalies, which drive our ice-sheet simulations, relative to the first or last 50 years of the corresponding piControl runs. If we alternatively compute the anomalies relative to the first 30 years of the transient historical period (1850–2005), we obtain also slightly different results. However, all these differences do not changes the spatial structure significantly, and they have a neglectable impact compared to the choice of the driving model.

The scaling across all model tends to be highest for the EAIS, where the part facing the Atlantic Ocean exhibits highest scalings (Figure 5). The WAIS has a lower scaling and the embedded region “Siple Coast” has on average the lowest scaling. There is a tendency for a higher scaling under a more vigorously changing climate across all regions, except for the smallest region “Ross.” This tendency exists for the ensemble mean and across models characterized by a larger than average scaling. The detected precipitation deficit in reanalysis data and shallow ice cores in the “Siple Coast” region (Wang et al., 2017) is represented by most models by a reduced scaling, while only NorESM1-M shows a precipitation deficit under a raising air temperature for all future climate scenarios. When considering the whole Antarctica, the difference between the grounded ice sheet only and all glaciated regions (including ice shelves) is small.

The highest scaling spread between the first and last 50 years piControl reference period has MIROC-ESM across all inspected regions and scenarios, which is probably related to the pronounced trend of the global 2m-air temperature (0.67°C) between these two reference periods in our ensemble. Otherwise, the spread is related to enhanced/amplified long-term re-

https://doi.org/10.5194/esd-2019-78
Preprint. Discussion started: 6 January 2020

gional climate variability expressed by differing values in the reference period. For example, CCSM4 or MPI-ESM-LR are subject to a larger spread in the Atlantic sector of the EAIS, while in the neighboring Indian sector the variability is negligible. The higher spread of the smaller subregion Ross within the WAIS sector supports this interpretation (at least for the models CCSM4, CanESM2, HadGEM2-ESM).

There exists a tendency towards a higher scaling of coastal areas that are subject to incoming storm tracks, which potentially deliver heavier precipitation events that are also controlled by the rising topography height towards the interior of Antarctica. In the majority of the simulations, we identify a lower scaling in WAIS and also a low to negative scaling in the area of the Ross Ice Shelf and the adjacent parts of the WAIS.

A2 Marginal ice loss by ocean-driven basal melting and iceberg calving

We turn our analysis to the individual mass balance terms: Iceberg calving, basal melting in the ice-shelf cavities, and surface mass balance. To recap: the surface mass balance is obtained by applying the individual spatial atmospheric model forcing on top of the reference fields obtained from RACMO, while the basal melting is calculated by adding ocean anomalies on top of the World Ocean Atlas climatology (Table 2). The calving is composed of three processes (thickness calving, Eigen-calving, kill mask calving) as part of the Parallel Ice Sheet Model (PISM) simulations. Here, the analysis focuses predominantly on the period from 1850 to 2100, because after 2100, we reapply the forcing from 2071–2100 recurrently.

Until 2100, the temporal evolution of the iceberg calving rates of individual ensemble members is subject to some variability, which is typical for such event-based mass losses. For some models, we could identify some reduced calving of $20\,\%$ around 1850 and 1970, and some enhanced calving of $25\,\%$ around 1920 and 2050. These trends are noisy and are independent of the applied forcing scenario RCP2.6, RCP4.5, and RCP8.5 (Figure A12). Overall, the temporal evolution of the calving does not show a clear trend, and the average calving loss rate of the entire ensemble is about $5500\,\mathrm{Gt\,year^{-1}}$ (Figure A12). Clearly separated are the calving rates of ensemble members starting from either the initial state PISM1Eq or PISM2Eq. The members of the group starting from PISM1Eq have on average a calving rate of approximately $7500\,\mathrm{Gt\,year^{-1}}$, while it amounts to about $3500\,\mathrm{Gt\,year^{-1}}$ in the PISM2Eq. So a reduction of the Eigen-calving constant by an order of magnitude from 10^{18} (PISM1Eq) to 10^{17} (PISM2Eq) halves approximately the total calving rate, while in both cases the thickness calving is active for marginal ice-shelf point with a thickness of less than $150\,\mathrm{m}$.

Iceberg calving and basal ice-shelf melting control the overall mass loss of Antarctica, while the relative contribution is unclear. Depoorter et al. (2013) report a nearly equal share between calving ($1321 \pm 144\,\mathrm{Gt\,year^{-1}}$) and basal melting ($1454 \pm 174\,\mathrm{Gt\,year^{-1}}$), Rignot et al. (2013) detect a slightly higher contribution from basal melting ($1325 \pm 235\,\mathrm{Gt\,year^{-1}}$ compared to calving with $1089 \pm 139\,\mathrm{Gt\,year^{-1}}$), while Liu et al. (2015) find that the basal melting ($1516 \pm 106\,\mathrm{Gt\,year^{-1}}$) contribution is twice as much as the calving ($755 \pm 24\,\mathrm{Gt\,year^{-1}}$) contribution. Both ensemble branches starting from PISM1Eq and PISM2Eq overestimate the currently observed calving rates of less than $1500\,\mathrm{Gt\,year^{-1}}$ (Depoorter et al., 2013; Liu et al., 2015; Rignot et al., 2013). Also the combined observed mass loss by calving and basal melting of ice shelves, which is about $2500\,\mathrm{Gt\,year^{-1}}$ (Depoorter et al., 2013; Liu et al., 2015; Rignot et al., 2013), is on average smaller than the lower simulated

https://doi.org/10.5194/esd-2019-78
Preprint. Discussion started: 6 January 2020


Earth System Dynamics Discussions Open Access EGU

calving rate from our ensemble members starting from PISM2Eq. Therefore, our ensemble mean ice loss rate exceeds current estimates, which could lead to an overestimation of the total sea-level rise in our simulations.

The basal melting rate of floating ice shelves, in the following just termed basal melting rates, is the second ice mass loss process. The basal melting rate anomaly is computed relative to the 50 years between 1951 and 2000. We could identify immediately that the basal melting rates have risen between $10\,\%$ and $100\,\%$ since the 1850s (Figure A13). The simulated historical trend is nearly independent of the initial state selection (PISM1Eq and PISM2Eq) and reference to compute the ocean temperature anomaly. For each climate model scenario, the anomalies are computed relative to the first or last 50 years of the pre-industrial climate (piControl) simulations. However, only for MIROC-ESM the reference state (first vs. last 50 years piControl) matters, because this model is subject to not negligible trend during the piControl phase.

In the future, the basal melting rate will further increase between $10\,\%$ and more than $100\,\%$. The latter increase is consistent with results from specialized ocean simulations. These simulations resolve ice shelves, include the ocean-ice-sheet interaction explicity, are driven by future projection from various climate models (Naughten et al., 2018; Hellmer et al., 2012).

The temporal evolution of the actual basal melting rate (Figure A13) increases until 2100 and falls back afterward onto the value of the year 2071 because we apply the last 30-years-forcing recurrently after 2100. Also, for the basal melting the separation of ensemble members starting from PISM1Eq and PISM2Eq is apparent. However, both groups are close to the ensemble mean, which is in contrast to the calving rate. The basal melting rates of all ensemble members underestimate the observational basal melting rates.

Since, in general, the observed calving rate is lower than the basal melting rate, our model ensemble swaps the importance of basal melting and iceberg calving. Also the sum of the calving rate and basal melting rate exceeds the observed estimates. Hence, our simulations could tend to overestimate ice loss and, ultimately, sea-level rise.

The ensemble mean calving and basal melting rates stay nearly constant or reach a maximum of around 2100 and scenarios with a higher forcing (RCP8.5 vs. RCP4.5, for instance) cause more ice loss by both calving and basal melting. Beyond 2100, ice loss rates decrease in general (Figure A14). Since the temporal variability remains high also after 2100, our approach works where the last 30 years of the forcing until 2100 is recurrently applied afterward. To highlight the primary trend in the temporal evolution after 2100, a 250-year running mean is applied after 2100.

The basal melting rates of the stronger forcing scenario RCP8.5 show a minimum of around 3500 and increase afterward slightly, while the other scenarios (RCP4.5 and RCP2.6) indicate a tendency for stabilization at the end of our simulation in the year 5000 (Figure A14). Over the entire period, the basal melting rate is higher for the stronger forcing scenarios. This result reflects the dependence of the basal melting on the ocean temperature because the ocean temperature anomalies are warmer for the scenarios with a higher forcing.

The calving rates before 2100 tend to be slightly higher for the RCP8.5 scenario. However, after 2100, we detect the sharpest fall of the ice loss rates for the scenario RCP8.5 and an average decrement for RCP4.5 and a moderate reduction for RCP2.6 (Figure A14). Around 3000, RCP8.5 calving reaches its minimum, followed by an enhanced increase for 500 years and a moderate increase afterward. Forcing scenarios with a lower strength reach the minimum later, so that RCP4.5 has its minimum around 3200, while RCP2.6 shows the minimum around 3700. At this time, the ensemble mean calving rates of the RCP4.5

https://doi.org/10.5194/esd-2019-78
Preprint. Discussion started: 6 January 2020


Earth System Dynamics Discussions Open Access EGU

and RCP2.6 are similar (please note that RCP2.6 does not include simulations driven by CCSM4). The trends of all scenarios converge around 4000.

In the long term, the most active basal melting occurs for the stronger forcing scenarios, while the highest calving occurs under scenarios with a lower forcing. The calving rate controls the evolution of the total ice mass loss in our simulations. Before the year 2100, RCP8.5 has the highest calving rates, while these are lowest shortly afterward. The ordering of the scenarios with the highest calving rates (RCP2.6) is those with the lowest forcing (RCP2.6) and vise versa (RCP8.5). The ensemble mean of the basal melting increases by 60 %–70 %, 70 %–85 %, and 90 %–115 %, for RCP2.6, RCP4.5, and RCP8.5, respectively. The fractional calving change of the ensemble mean is between $+2\,\%-\,-4\,\%$, $+2\,\%-\,-10\,\%$, and $+2\,\%-\,-19\,\%$ for RCP2.6, RCP4.5, and RCP8.5, respectively. Across these, we detect that the most substantial ice-shelf area reduction occurs for RCP8.5 and the lowest for RCP2.6. Our simulations suggest that the warmer climate causes a stronger ice-shelf retreat and a stronger drop in the calving rate in the period, where the ice shelf could adjust to the quasi-equilibrium forcing. Based on these results we conclude: warmer climate drives more basal melting and enhances calving so that we obtain smaller ice shelves. Under the assumption that the smaller total integral of the ice shelves area is proportional to the calving probability (under else nearly unaltered conditions), we ultimately reduce the calving rates.

A3 Bias-corrected fluxes

Starting from original simulated ablation flux F_{org}, which could be the basal melting flux $F^B_{\mathrm{org}}(t)$ or the iceberg discharge flux $F^D_{\mathrm{org}}(t)$, and the corresponding reference flux $F_{\mathrm{ref}}(t_{\mathrm{ref}})$ at time t_{ref}, we define the following ratios. The fraction of the temporal evolving flux ($F_{\mathrm{org}}(t)$) to the original flux at the reference time (t_{ref}):

$$r(t) = \frac{F_{\mathrm{org}}(t)}{F_{\mathrm{org}}(t_{\mathrm{ref}})} \implies r(t_{\mathrm{ref}}) = 1, \tag{A1}$$

and the fraction of the original simulated flux to the reference flux (F_{ref})

$$q = q(t_{\mathrm{ref}}) = \frac{F_{\mathrm{ref}}(t_{\mathrm{ref}})}{F_{\mathrm{org}}(t_{\mathrm{ref}})}. \tag{A2}$$

The corrected flux F_{cor} using Equation A1 is defined as

$$F_{\mathrm{cor}}(t) = r(t) \cdot F_{\mathrm{ref}}(t_{\mathrm{ref}}), \tag{A3}$$

so that the flux difference $\Delta F(t)$ is

$$\begin{aligned}\Delta F(t) &= F_{\mathrm{cor}}(t) - F_{\mathrm{org}}(t) \\ &= F_{\mathrm{org}}(t)\left[\frac{F_{\mathrm{ref}}(t_{\mathrm{ref}})}{F_{\mathrm{org}}(t_{\mathrm{ref}})} - 1\right].\end{aligned}$$

With Equation A2 we obtain

$$\Delta F(t) = F_{\mathrm{org}}(t)\,[q-1]\,. \tag{A4}$$

https://doi.org/10.5194/esd-2019-78
Preprint. Discussion started: 6 January 2020


Earth System Dynamics Discussions Open Access EGU

The ratio $p(t)$ of the sea level temporal deviation to the ice mass temporal deviation is

$$p(t) = \frac{\frac{dz_l(t)}{dt}}{\frac{dm_{\mathrm{ice}}(t)}{dt}}, \tag{A5}$$

where z_l is the sea level and m_{ice} the total ice mass, which includes grounded and floating ice. We use here $p = \mathrm{median}(p(t))$ so that each ensemble member is characterized by one value for its entire time series. If $p = \frac{1}{\rho A_{\mathrm{oce}}}$, $100\,\%$ of flux difference (Equation A4) contributes immediately to the sea level of the global ocean with an area of A_{oce}.

The total ice mass (m_{ice}) changes are driven by four terms

$$\frac{m_{\mathrm{ice}}}{dt} = \underbrace{\left[F^{SMB}(t) + F^{G}(t)\right]}_{\text{unchanged under correction}} + F^{B}(t) + F^{D}(t),$$

where $F^{SMB}(t)$ is the surface mass balance flux and $F^{G}(t)$ the basal mass flux of grounded ice (Figure A9). We assume that these two terms in the brackets do not change regardless of the applied corrections to the last two terms F^{B} and F^{D}. Hence the difference in the ice mass change is

$$\Delta\frac{dm_{\mathrm{ice}}}{dt} = \Delta F^{B}(t) + \Delta F^{D}(t) \tag{A6}$$

Now we relate the temporal evolution of the sea level to the total ice mass changes by utilizing the Equation A5

$$\frac{z_{l\mathrm{cor}}}{dt} = \frac{z_{l\mathrm{org}}}{dt} + p(t) \cdot \left[\Delta F^{B}_{\mathrm{cor}}(t) + \Delta F^{D}_{\mathrm{cor}}(t)\right],$$

so that we obtain:

$$z_{l\mathrm{cor}} = z_{l\mathrm{org}} + \Delta z_l(t), \tag{A7}$$

where the sea-level difference $\Delta z_l(t)$ is

$$\Delta z_l(t) = \int_{t_0}^{t} p(\hat{t}) \left[\Delta F^{B}_{\mathrm{cor}}(\hat{t}) + \Delta F^{D}_{\mathrm{cor}}(\hat{t})\right] d\hat{t}. \tag{A8}$$

The Figures A5 and A7 depict the sea-level difference for two cases. If the additional mass loss contributes immediately to a rising sea level (Figure A7), the sea level rise of $30\,\mathrm{cm}$ is larger than the actual sea level rise since 1850 of about $20\,\mathrm{cm}$ (Church and White, 2011).This case is not realistic because a melting floating ice shelf does not impact the sea level. Only the flow of grounded ice across the grounding line to feed an ice shelf or the direct loss of grounded ice rise the sea level.

In contrast, the sea level changes hardly (Figure A5) if the deduced ratio $\overline{p(t)}$ (Equation A5), which corresponds to the ratio defined in Equation A5. It is computed for each ensemble mean as median of its time series. If the ratio between ice loss and sea-level rise is constant under amplified basal melting of ice shelves is an open question. Strongly intensified ocean-driven ice

https://doi.org/10.5194/esd-2019-78
Preprint. Discussion started: 6 January 2020


Earth System Dynamics
Discussions
Open Access
EGU

loss will probably cause a retreating grounding line on a longer time scale, which ultimately releases grounded ice into the sea and increases the sea level.

Figure A8 shows the proportion of the deduced ratio to the $100\,\%$ ratio. Only very few ensemble member losses about 15% of the maximum value of $p = 1/(\rho \cdot A_{\mathrm{oce}})$. In contrast, the mean and median value of this proportion is generally less then $5\,\%$. For all ensemble members driven by the precipitation anomaly, this proportion is on average $4.7\,\%$ with a median of $3.9\,\%$. It is even lower for ensemble members driven by the temperature scaled precipitation. The median amounts $0.7\,\%$ and the corresponding mean is $0.9\,\%$. Please note that some ensemble members under the temperature scaled precipitation are subject to a negative scaling. This result confirms the above presented low positive and negative scaling seen for restricted regions (Figure 5). It highlights also that simulations driven by temperature scaled precipitation could show unexpected results.

https://doi.org/10.5194/esd-2019-78
Preprint. Discussion started: 6 January 2020

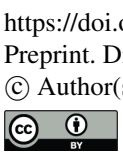

Earth System Dynamics
Discussions
Open Access
EGU

A4 Appendix Figures

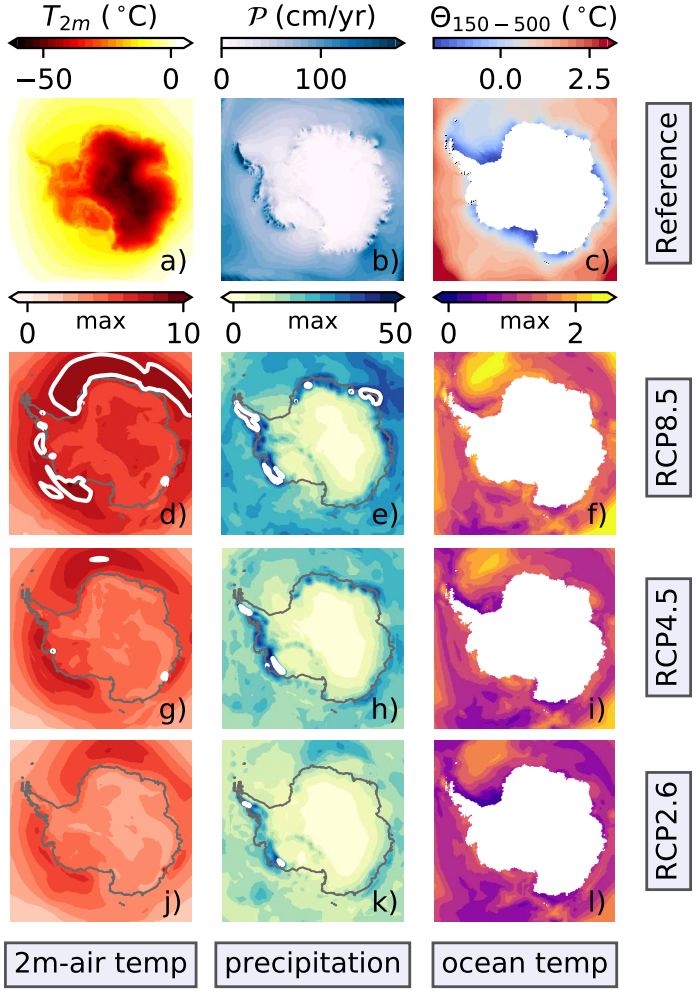

Figure A1. Atmospheric (a, b) and oceanographic (c) reference forcing; ensemble maximum anomalies (d–l). The top row represents the reference fields to spin-up the ice-sheet model (Table 2). The 2m-air temperature (a) and the total precipitation (b) are mean fields from the regional RACMO model, while the ocean temperatures come from the World Ocean Atlas 2009 (c). Below each reference field, the related maximum anomalies are compiled for the period 2071–2100. Here, the second (third and fourth) row shows the anomalies for RCP8.5 (RCP4.5, RCP2.6). The dark-gray line follows the current coastline. All potential ocean temperatures (c, f, i, l) are a vertical mean of the depth interval from 150 m to 500 m. The white contour lines in the anomaly plots highlight the following thresholds. 2m-air temperature (d, g, j): 8°C; total precipitation (e, h, k) $50\,\mathrm{cm\,year^{-1}}$. All these anomalies are the ensemble maximum of the models listed in Table 1; please note that CCSM4 is not part of RCP2.6. Figure 2 shows the corresponding ensemble mean fields.

https://doi.org/10.5194/esd-2019-78
Preprint. Discussion started: 6 January 2020

Earth System Dynamics
Discussions
Open Access
EGU

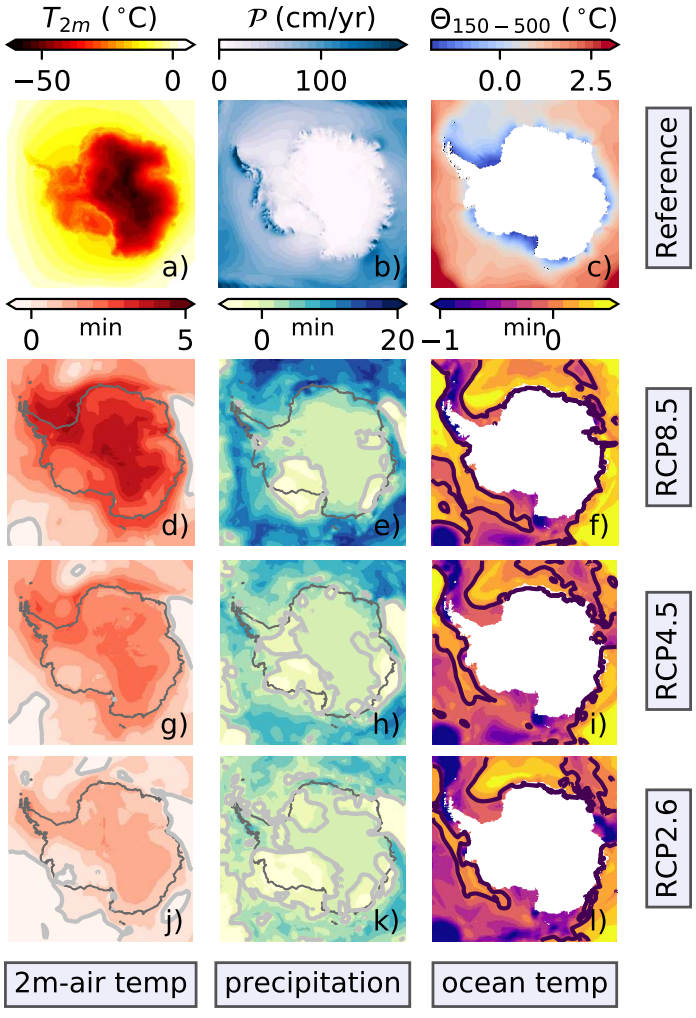

Figure A2. Atmospheric (a, b) and oceanographic (c) reference forcing; ensemble minimum anomalies (d–l). The top row represents the reference fields to spin-up the ice-sheet model (Table 2). The 2m-air temperature (a) and the total precipitation (b) are mean fields from the regional RACMO model, while the ocean temperatures come from the World Ocean Atlas 2009 (c). Below each reference field, the related minimum anomalies are compiled for the period 2071-2100. Here, the second (third and fourth) row shows the anomalies for RCP8.5 (RCP4.5, RCP2.6). The dark-gray line follows the current coastline. All potential ocean temperatures (c, f, i, l) are a vertical mean of the depth interval from 150 m to 500 m. The white-grey lines in the anomaly plots highlight the following thresholds. 2m-air temperature (d, g, j): 0°C; total precipitation (e, h, k) $0\,\mathrm{cm\,year^{-1}}$; potential ocean temperature 0°C. All these anomalies are the ensemble minimum of the models listed in Table 1; please note that CCSM4 is not part of RCP2.6. Figure 2 shows the corresponding ensemble mean fields.

https://doi.org/10.5194/esd-2019-78
Preprint. Discussion started: 6 January 2020

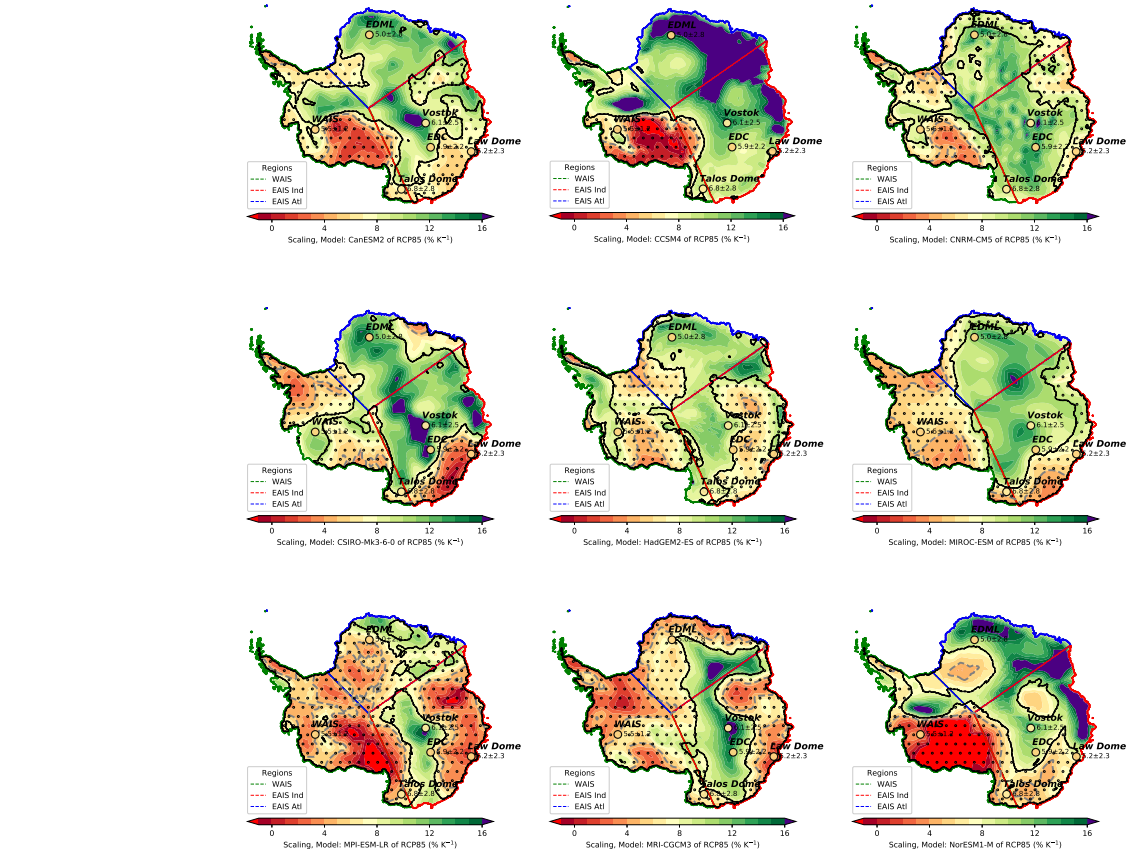

Figure A3. Temperature scaled precipitation under the RCP8.5 scenario for nine CMIP5 models (Table 1): Period 2051–2100. The ice-sheet simulations are driven by anomalies relative to the first 50 years of the related piControl climate scenario. In the dotted regions enclosed by black contours, the combined simulated scaling and the standard deviation contains the value of $5\,\%\mathrm{K}^{-1}$. Gray dashed lines follow this $5\,\%\mathrm{K}^{-1}$ contour. The scaling values deduced from ice cores are shown at their location (mean and the 2-sigma uncertainty). The regions named "WAIS," "EAIS Atl," and "EAIS Ind" are outlined by their green, blue, and red, respectively, boundaries (lower left legend). For further details, inspect the text, please. Figure 4 shows the corresponding ensemble mean. The contours of the Antarctic continent are deduced from Fretwell et al. (2013).

https://doi.org/10.5194/esd-2019-78
Preprint. Discussion started: 6 January 2020

Earth System Dynamics
Discussions
Open Access
EGU

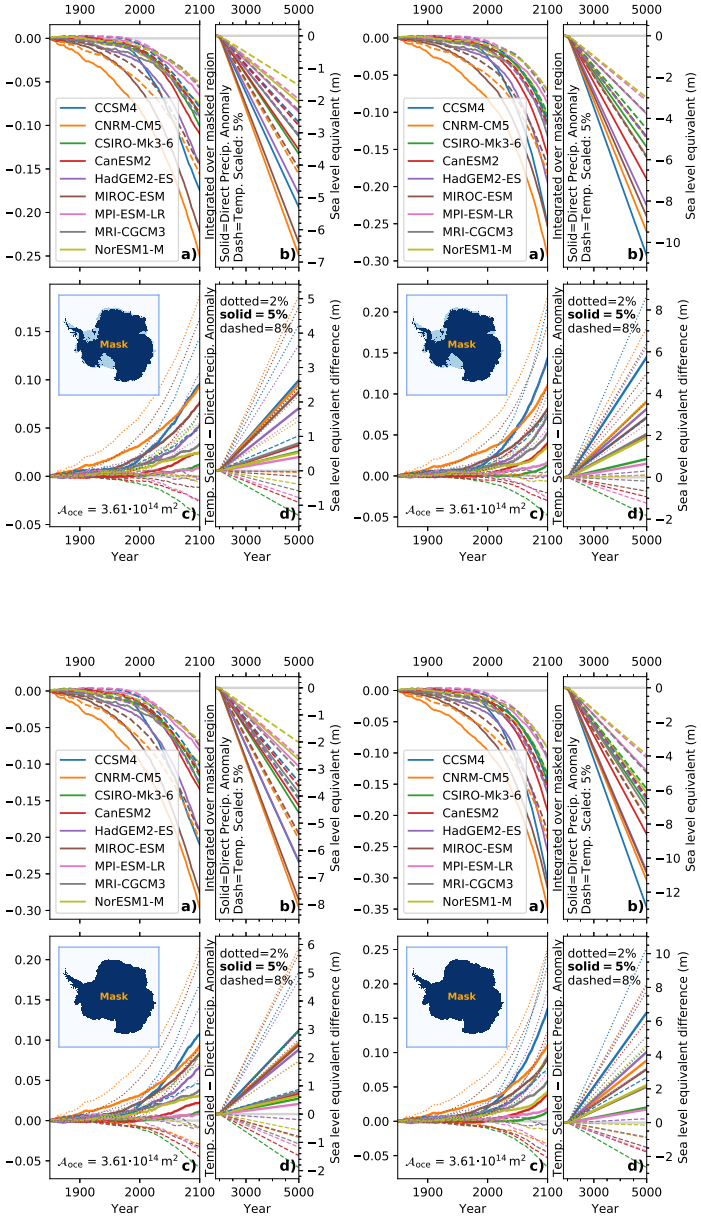

Figure A4. Integrated sea-level equivalent of the precipitation falling on Antarctica (see the mask in each subpanel) from the anomaly forcing (a, b: solid lines) and temperature scaled precipitation (a, b: dashed lines). The sea-level impact between the anomalies and the temperature scaled precipitation (c, d) is depicted for each CMIP5 model (legend on the lower left). The subpanels in the left and right columns show the results under the RCP4.5 and RCP8.5 scenarios, respectively. The upper row depicts the scaling for the entire Antarctic continent ("glaciered"), while the lower row is restricted to grounded ice. The lower left subpanel is identical to Figure 6. Please inspect this figure for further details. The grounded and floating ice areas are derived from Fretwell et al. (2013)

https://doi.org/10.5194/esd-2019-78
Preprint. Discussion started: 6 January 2020

Earth System Dynamics
Discussions
Open Access
EGU

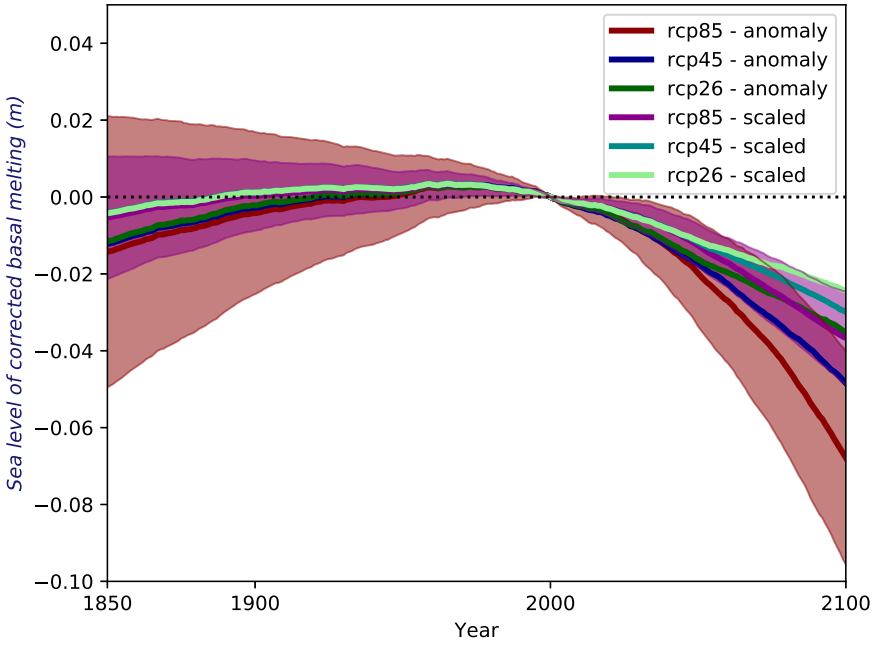

Figure A5. The diagnosed sea level correction as defined by Equation A8 covers the period from 1850 until 2100. Here, the ratio $p(t)$ (Equation A5) is the temporal median for each ensemble member (please see Figure A7 for the corresponding figure, where all additional mass loss rises immediately the sea level). The correction is computed relative to the year 2000 as in Figure 12. The resulting sea level for the entire period from 1850 until 5000 depicts the Figure A6. As reference value for the basal melting rate $F^B_{\mathrm{ref}}(t_{\mathrm{ref}})$, we use $1431\,\mathrm{Gt\,year^{-1}}$, which corresponds to the estimate of Depoorter et al. (2013) with $1454 \pm 174\,\mathrm{Gt\,year^{-1}}$, while it falls below the values of Liu et al. (2015) ($1516 \pm 106\,\mathrm{Gt\,year^{-1}}$), but is also exceed the rate of $1325 \pm 235\,\mathrm{Gt\,year^{-1}}$ reported by Rignot et al. (2013); our reference $F^B_{\mathrm{ref}}(t_{\mathrm{ref}})$ corresponds to the mean of all these basal melting estimates: $1431\,\mathrm{Gt\,year^{-1}}$.

https://doi.org/10.5194/esd-2019-78
Preprint. Discussion started: 6 January 2020

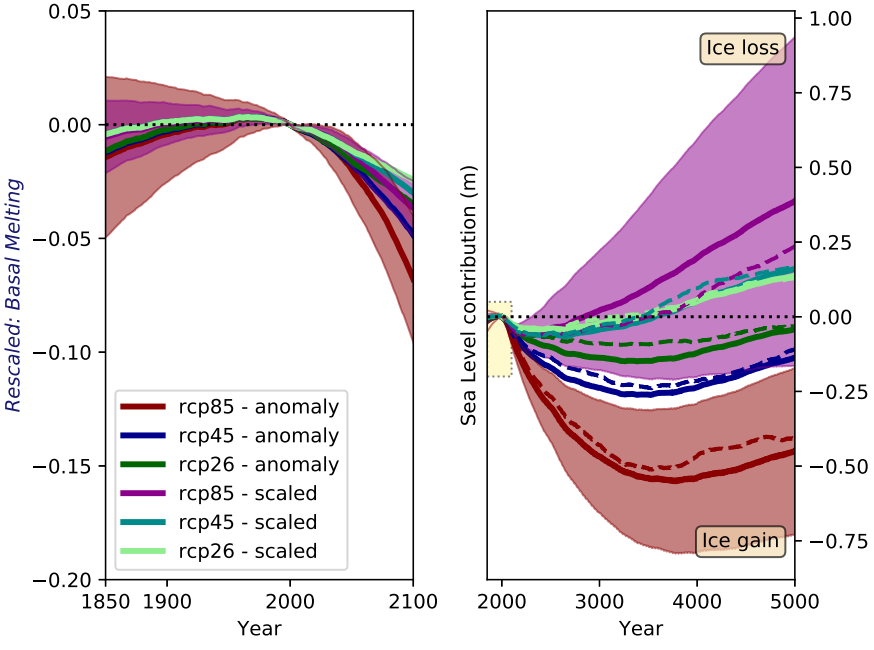

Figure A6. The sea level considering the correction as defined by Equation A8 and Figure A5. The sea level is is computed relative to the year 2000 as in Figure 12. Please inspect the Figure 12 for further details.

https://doi.org/10.5194/esd-2019-78
Preprint. Discussion started: 6 January 2020

Earth System Dynamics
Discussions
Open Access
EGU

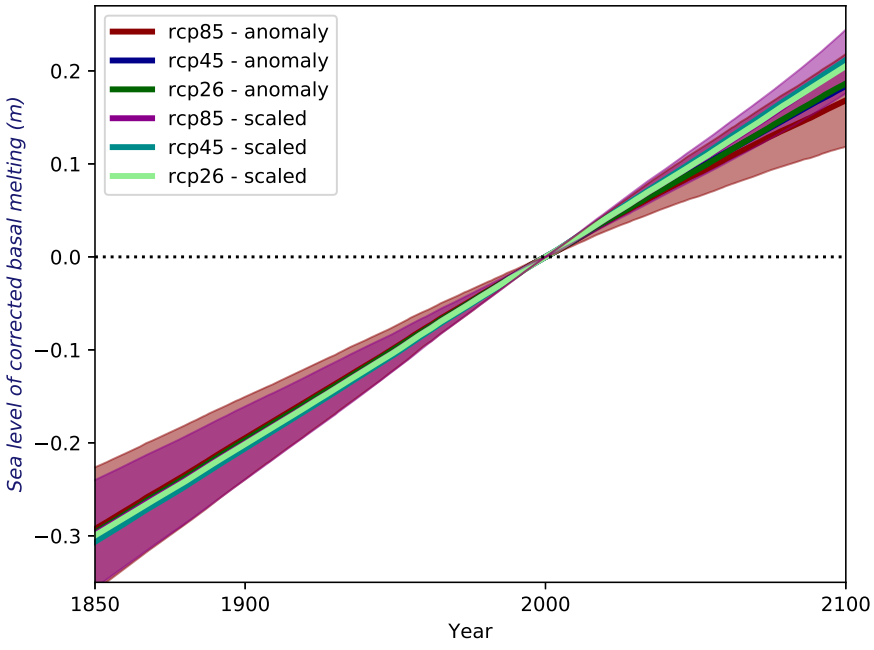

Figure A7. The diagnosed sea level correction as defined by equation A8 covers the period from 1850 until 2100, where $100\,\%$ of the additional mass loss contributes immediately to a rising sea level, hence the ratio p (Equation A5) equals $p = 1/(\rho A_{\mathrm{oce}})$. The correction is computed relative to the year 2000 as in Figure 12. The corresponding Figure A5 depicts the case where the correction considers the actual deduced ratio $p(t)$ of the each ensemble member.

https://doi.org/10.5194/esd-2019-78
Preprint. Discussion started: 6 January 2020

Earth System Dynamics
Discussions
Open Access
EGU

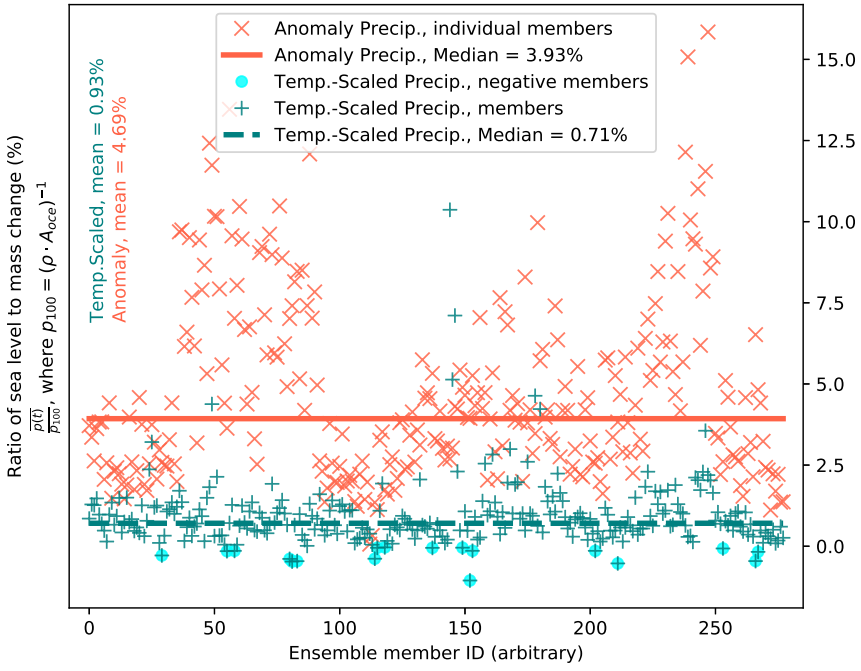

Figure A8. The ratio between the actual sea level contribution due to mass loss and the sea level equivalent of corresponding mass. Individual ensemble members are shown as crosses. A red "x" represents a member that is driven by the precipitation anomaly, while a blue-green "+" indicates those driven by the temperature scaled precipitation. In the latter case, light blue circles highlight members with negative ratios. Vertical lines mark median values for these two groups; see also legend. The corresponding mean values are listed on the left side. The term $\overline{p(t)}$ is defined by the Equation A5 and $p_{100} = \frac{1}{\rho \cdot A_{\mathrm{oce}}}$, where ρ is the density and A_{oce} represents the global ocean area.

https://doi.org/10.5194/esd-2019-78
Preprint. Discussion started: 6 January 2020

Earth System Dynamics
Discussions
Open Access
EGU

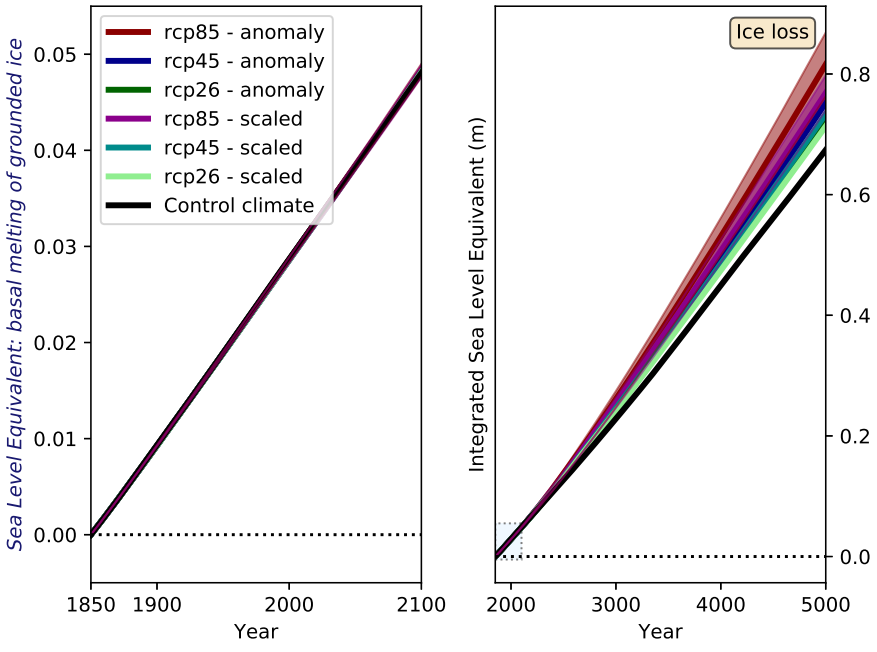

Figure A9. Cumulated basal melting of grounded ice as sea level equivalent. Shown are the results of the entire ensemble of ice-sheet simulations. The solid lines represent the ensemble averages for the applied precipitation anomalies and the temperature-scaled precipitation boundary conditions according to the legend (lower left). For the RCP8.5 scenario, the shading highlights the standard deviation (1-sigma) as a measure of the variability among the ice-sheet ensemble members driven by various climate models (Table 1).

https://doi.org/10.5194/esd-2019-78
Preprint. Discussion started: 6 January 2020

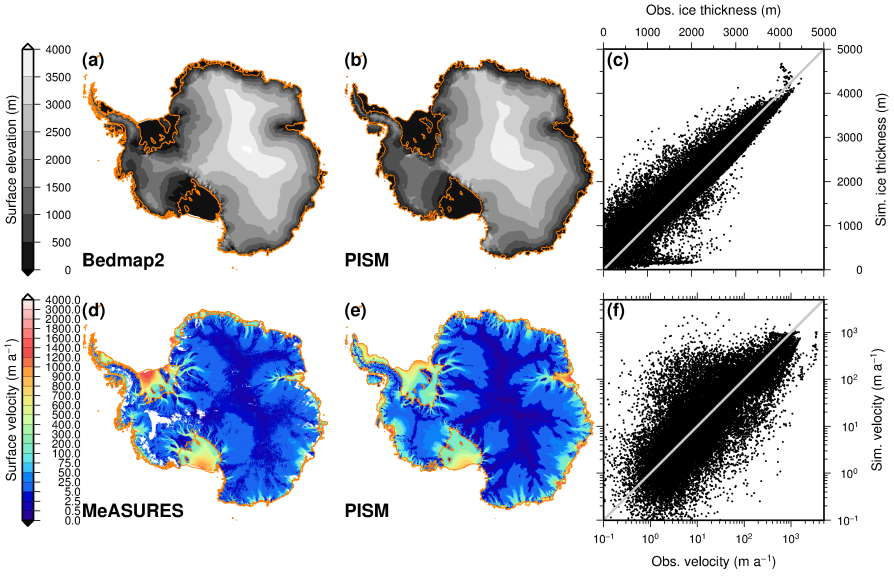

Figure A10. Comparison between the initial state PISM1Eq and observational estimates. The top row depicts the surface elevation: a) Bedmap2 data set (Fretwell et al., 2013), b) simulated ice elevation in PISM and c) point-wise comparison. The lower row shows the surface velocity distribution: d) Observations (Rignot et al., 2016), e) simulation and f) point-wise comparison; please note that both axes are logarithmic. For the point-wise comparison, the observations follow the x-axis (abscissa) while simulated values follow the y-axis (ordinate).

https://doi.org/10.5194/esd-2019-78
Preprint. Discussion started: 6 January 2020

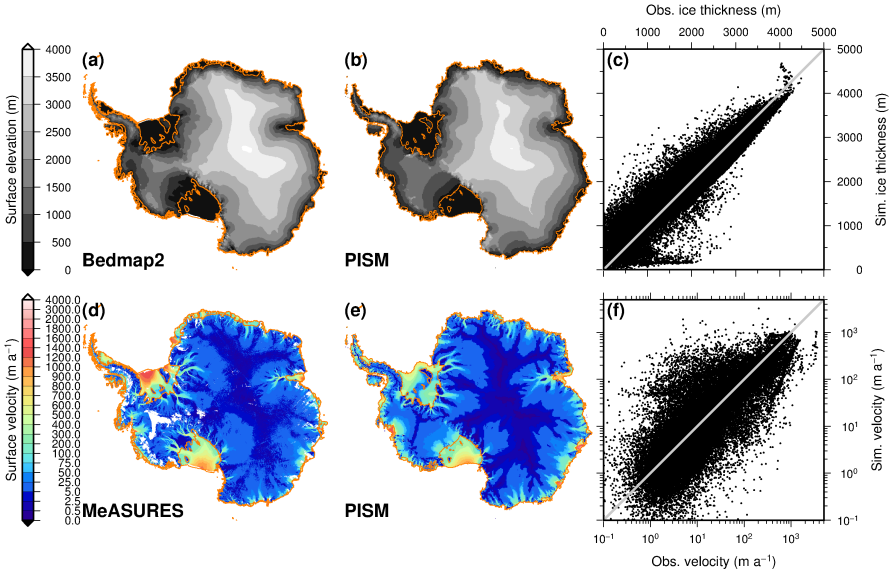

Figure A11. Comparison between the initial state PISM2Eq and observational estimates. The top row depicts the surface elevation: a) Bedmap2 data set (Fretwell et al., 2013), b) elevation in PISM and c) point-wise comparison, while the lower row shows the surface velocity: d) Observations (Rignot et al., 2016), e) simulation and f) point-wise comparison. Please see also Figure A10 (PISM1Eq) for further details.

https://doi.org/10.5194/esd-2019-78
Preprint. Discussion started: 6 January 2020

Earth System Dynamics
Discussions
Open Access
EGU

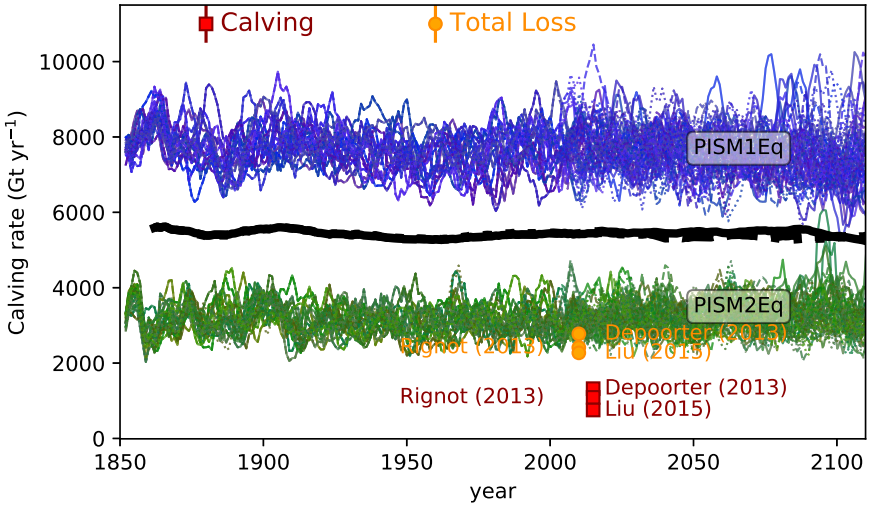

Figure A12. Temporal evolution of Antarctic-wide calving rates for the period from 1850 to 2100. The thin blue lines are all ensemble members starting from the initial state PISM1Eq, where the Eigen-calving parameter amounts 10^{18}, while the green lines are the corresponding simulations starting from PISM2Eq (Eigen-calving parameter 10^{17}). A running mean with a window of 5 years has been applied for the thin lines. All simulations start under historical conditions and continue after 2005 under the RCP8.5 (solid lines), RCP4.5 (dashed lines) or RCP2.6 (dotted lines) scenario. The thick black lines represent the ensemble mean of the three future scenarios with a moving window of 25 years. Recent estimates of the total (orange circles) and the calving (red squares) ice mass loss are given for three studies (legend at the top). Vertical bars depict the reported uncertainties of the shown estimates by Liu et al. (2015); Depoorter et al. (2013); Rignot et al. (2013).

https://doi.org/10.5194/esd-2019-78
Preprint. Discussion started: 6 January 2020

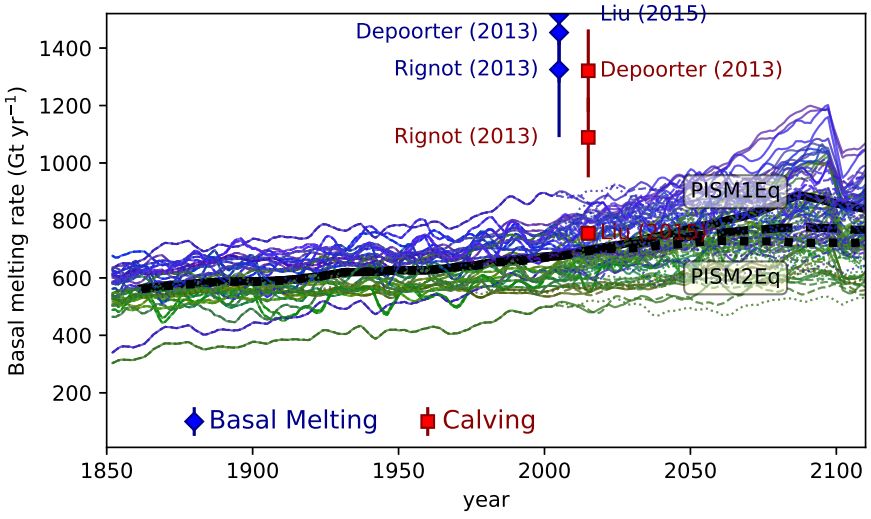

Figure A13. Temporal evolution of the basal melting rates in fringing ice shelves around Antarctica for the period from 1850 to 2100. The thin blue lines are all ensemble members starting from the initial state PISM1Eq, where the Eigen-calving parameter amounts 10^{18}, while the green lines are the corresponding simulations starting from PISM2Eq (Eigen-calving parameter 10^{17}). A running mean with a window of 5 years has been applied for the thin lines. All simulations start under historical conditions and continue after 2005 under the RCP8.5 (solid lines), RCP4.5 (dashed lines) or RCP2.6 (dotted lines) scenario. The thick black lines represent the ensemble mean of the three future scenarios with a moving window length of 25 years. Recent estimates of the basal melting (blue diamonds) and the calving (red squares) ice mass loss are given for three studies (legend at the bottom, Liu et al. (2015); Depoorter et al. (2013); Rignot et al. (2013)). Related uncertainties are given as vertical lines if the uncertainties are larger than the symbol size.

https://doi.org/10.5194/esd-2019-78
Preprint. Discussion started: 6 January 2020

Earth System Dynamics
Discussions
Open Access
EGU

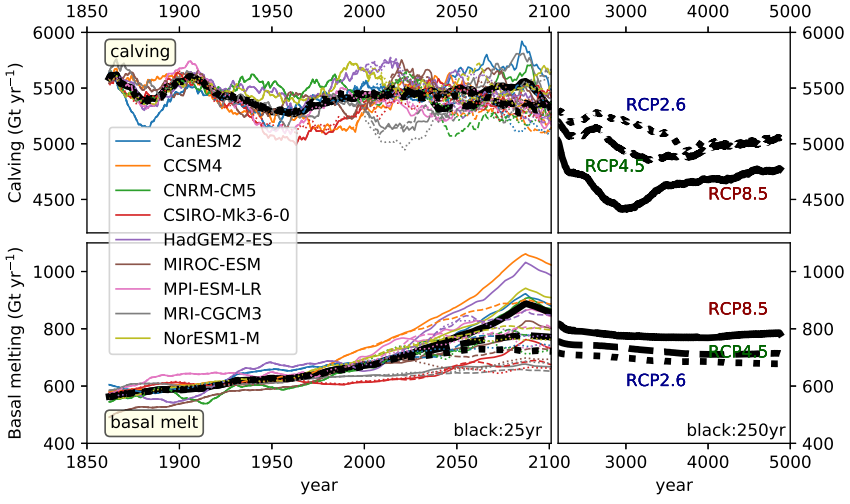

Figure A14. Long-term temporal evolution of the ensemble mean basal melting and calving ice loss rates from 1850 to 2100 and beyond until the year 5000. The upper panels show the calving rates, while the lower panels depict the basal melting rates. In the left columns, individual model simulations (colored lines according to the legend) are grouped together, while the thick black lines are the overall means as shown in the corresponding figures Figure A12 and A13. For the ensemble means of the period 1850–2100, a smoothing with a moving window of 25 years is applied (left column), while the smoothing window length is 250 years for the right column covering the period from 2100 until 5000. Solid (dashed, dotted) lines represent the RCP8.5 (RCP4.5, RCP2.6) scenario.

https://doi.org/10.5194/esd-2019-78
Preprint. Discussion started: 6 January 2020

Earth System Dynamics
Discussions
Open Access
EGU

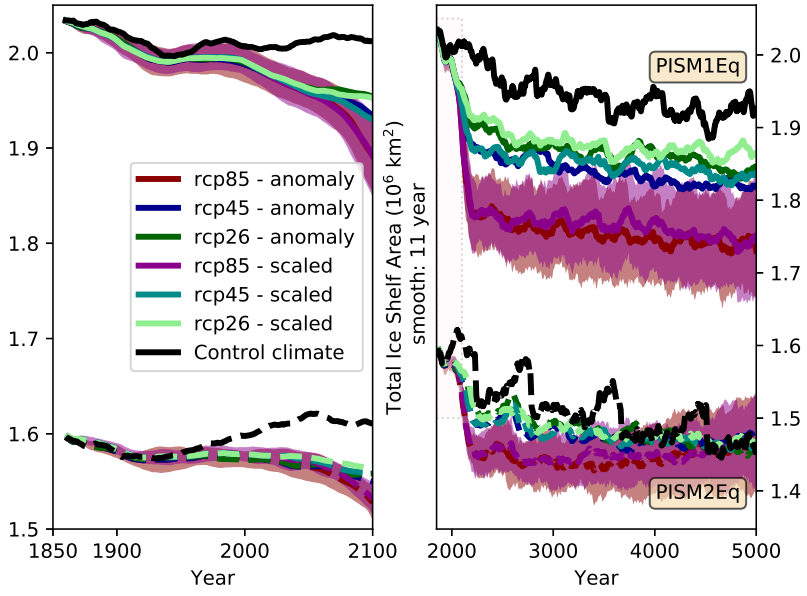

Figure A15. Area of floating ice shelves. A running mean window of 11 years is used for the entire ensemble of ice-sheet simulations. The solid lines represent the ensemble averages for the PISM1Eq starting conditions, while the dashed lines are the corresponding PISM2Eq condition. For the RCP8.5 scenario, the shading highlights the standard deviation (1-sigma) as a measure of the variability among the ice-sheet ensemble members driven by various climate models (Table 1). Please note the different axes for both subfigures. The dashed frame in the right subfigure depicts the value range of the left subfigure.